SSRG International Journal of Civil Engineering
ISSN: 2348-8352/https://doi.org/10.14445/23488352/IJCE-V10I7P101

Volume 10 Issue 7, 1-28, July 2023

Original Article

Optimizing the Design of Monolithic Dome Components to Withstand Combined Bending and Compressive Forces using Aluminium 6082-T6 Alloy

Guy Oyéniran ADEOTI[1], Peace Sena HOUNKPE[2], Judicael Koffi AGBELELE[3], Ogoubi Cyriaque ASSOGBA[4], Feng FAN[5]

[1,2,3,4]*Laboratory of Testing and Studies in Civil Engineering (L2EGC), National University of Science, Technology, Engineering, and Mathematics (UNSTIM), Department of Zou, Goho Abomey, Republic of Benin.*
[1,5]*School of Civil Engineering, Harbin Institute of Technology, Haihe Road, Nangang District, Harbin, PR China.*

[1]*Corresponding Author : adeotiguy@unstim.bj*

Received: 15 April 2023 Revised: 20 June 2023 Accepted: 10 July 2023 Published: 31 July 2023

Abstract *- In recent years, monolithic building solutions' durability, energy efficiency, and aesthetic appeal have contributed to their increasing popularity. However, it is crucial to diligently engineer these structures to prevent potential failures under various loads. The present work explores the engineering study of designing monolithic dome components using Aluminium 6082-T6 alloy. Material testing and connection moment capacity in semi-rigidly jointed structures are examined using experimental and finite element analysis (FEM) approaches. Two single-layered reticulated dome types of geometric and material nonlinear analysis (GMNA) were conducted. The domes were rigidly and semi-rigidly connected by incorporating Aluminium connection bending stiffness in an accurate and valid program. The resulting loads were used to determine the strength of the columns of the reticulated members of the dome. The coefficient of strength calculated was compared with the stability coefficients from different codes. This work also focuses on dimensioning structural elements under combined bending and buckling forces. It emphasizes incorporating second-order effects, buckling susceptibility, and spatial changes in axial force and flexural rigidity for accurate dimensioning. The proposed dimensioning criterion ensures the appropriate utilization ratio of the section by considering safety coefficients and critical loads*.

Keywords *- Buckling analysis, Dimensioning criteria for elements subjected to combined forces, Euler's law limitations, Rigid and semi- rigid joints, Structural design and optimization.*

1. Introduction

Dome structures have gained widespread use in engineering projects worldwide and have seen significant growth in recent years due to high-strength steel and advanced computer technology availability. Monolithic domes featuring semirigid joints are particularly noteworthy due to their reduced material usage, attractive appearance, and rapid construction with high accuracy. However, as dome spans increase significantly, instability issues can become critical, making understanding the factors influencing their stability essential. The study of instability in the architecture of monolithic dome structures is thus a relevant issue that requires thorough investigation.

1.1. Literature Review

During the 1900s, Timoshenko et al. studied structural members' buckling response. They derive analytical solutions for various types of members under different loading conditions and discuss the effects of geometric imperfections and material properties on buckling behaviour. Their works have become a foundational reference for the structural integrity assessment of elastic structures [1]. Stephen P. Timoshenko's "Theory of Elastic Stability" is a seminal and influential book covering the structural stability theory. It discusses buckling phenomena in columns, plates, and shells, in addition to the effects of initial imperfections.

The book explores critical load determination methods like the energy, Ritz, and Galerkin. Timoshenko's work has significantly shaped modern stability theory and is widely referenced in the field [2].

Forde et al. (1987) proposed an enhanced method for arc-length orthogonality in nonlinear finite element analysis. Their approach improves the traditional method's convergence efficiency by modifying the tangent stiffness matrix and residual vector. The method was validated through tests on various examples, demonstrating accelerated

convergence and reduced iteration requirements. It has since been widely adopted in nonlinear finite element analysis for improved efficiency and accuracy [3].

Reddy, J. N presents analytical and computational models for assessing buckling, vibration, and failure behaviour of laminated composite plates and shells and provides examples and problems for illustration [4]. Recently, researchers showed substantial interest in studying the structural integrity of dome structures. Researchers have utilized various methods to conduct such studies, including continuum shell analogy theories and finite element analysis, which have yielded significant insights into dome structures buckling critical force [5-7].

However, with the emergence of advanced finite element software and computer technology, there is potential for even more significant progress in instability research for dome structures. The popularity of nonlinear responses resulting from geometry and material characteristics investigation methods, such as GNA and GMNA, is growing as they replace traditional approaches, such as continuum shell analogy and finite element analysis. These new methods, coupled with using Eigenvalue and nonlinear buckling analyses, provide a deeper insight into the behaviour of single-layer domes [8-11].

S. Kato et al. introduce a method for determining suitable member sections of single-layer reticulated domes under varying loads, including uniform and non-uniform distributions.

The methodology relies on the nonlinear elasto-plastic buckling behaviour of the members, and it aims to achieve a cost-effective design while satisfying the structural safety requirements. The study concluded that the proposed methodology could effectively reduce the material cost of the structure while maintaining its safety and stability [12].

The ultimate load of monolithic domes is heavily influenced by joint inflexibility, which can be determined through testing and analytical models that provide insight into the joint moment-rotation behaviour. The analytical models consider various factors, including connection strength, rigidity, deformation capacity, and the nonlinear behaviour imposed by the material characteristics and shape. Fathelbab found that joint firmness profoundly affects load-displacement behaviour, highlighting the importance of understanding joint characteristics during the design stage to achieve optimal material usage and structure safety [13-16].

Researchers have recently investigated the buckling phenomenon of dome structures with semirigid connections. Murakami and Heki comprehensively analysed the instability under compression response of monolithic latticed domes with a regular hexagonal plan subjected to gravity load. They proposed a computational approach to study the buckling response and derived a general buckling equation for such domes.

The analysis considered the number of divisions, member slenderness ratio, and load direction. The study concludes that their theoretical approach helps design and analyzes latticed domes [17-21]. Yamada et al. investigated the overall buckling response of monolithic lattice domes under compression loading and the impact of initial geometric imperfections. Using finite element analysis, they analyzed different dome geometries and imperfection shapes. The study revealed that initial geometric imperfections significantly influenced the buckling strength, with critical imperfection shapes varying depending on the dome's geometry.

The authors provided design guidelines to enhance overall buckling strength by managing initial geometric imperfections [22]. Fan et al. (2012) studied the elasto-plastic structural integrity of monolithic lattice domes with initial member curvature. Their article suggested a computational method to evaluate the critical load, considering factors such as the slenderness ratio.

Numerical simulations validate their approach and provide insights for designing and analyzing such domes to investigate the structural integrity of lattice shells by analyzing the buckling of individual members. Their numerical method considers factors like span-to-height ratio and member slenderness.

The study emphasizes the significance of accounting for member buckling in accurately predicting the structural integrity of lattice shells [23]. To the best of our knowledge, until 2005, the design method for studying the instability of domes assumed that each member was straight and did not consider the pre-bending of the members. However, during the members' production, transportation, handling, and assembly, they inevitably become curved in one way or another, which can visibly reduce their ability to sustain load, provoking structural instability and damaging impacts, especially for compressed, slender members. Therefore, considering the pre-bending of members in the study of network-like shell structure instability is necessary. Subsequently, researchers started focusing on member and complete structure buckling [24-28].

Prior to 2012, there was insufficient research conducted on how buckling of the structural elements affects dome structures, and the matter had not been systematically explored because of insufficient engineering application results. Investigating the influence of buckling phenomena exhibited by structural members and complete buckling on dome structures is essential in nonlinear studies and in assessing member buckling assessment methods.

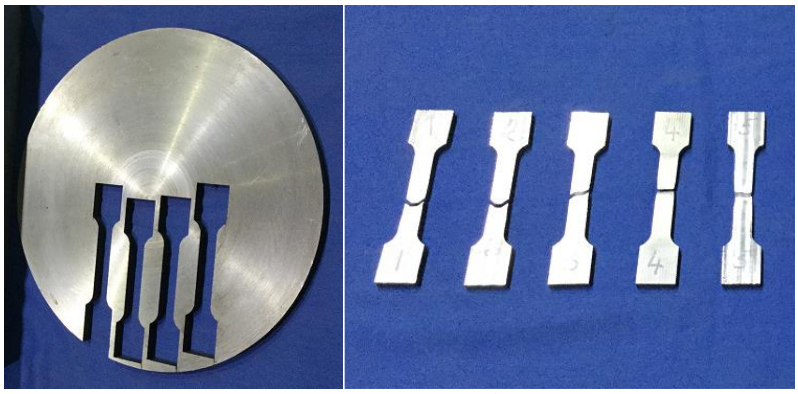

Fig. 1 Aluminium material tensile test coupons from Al. 6082-T6 body

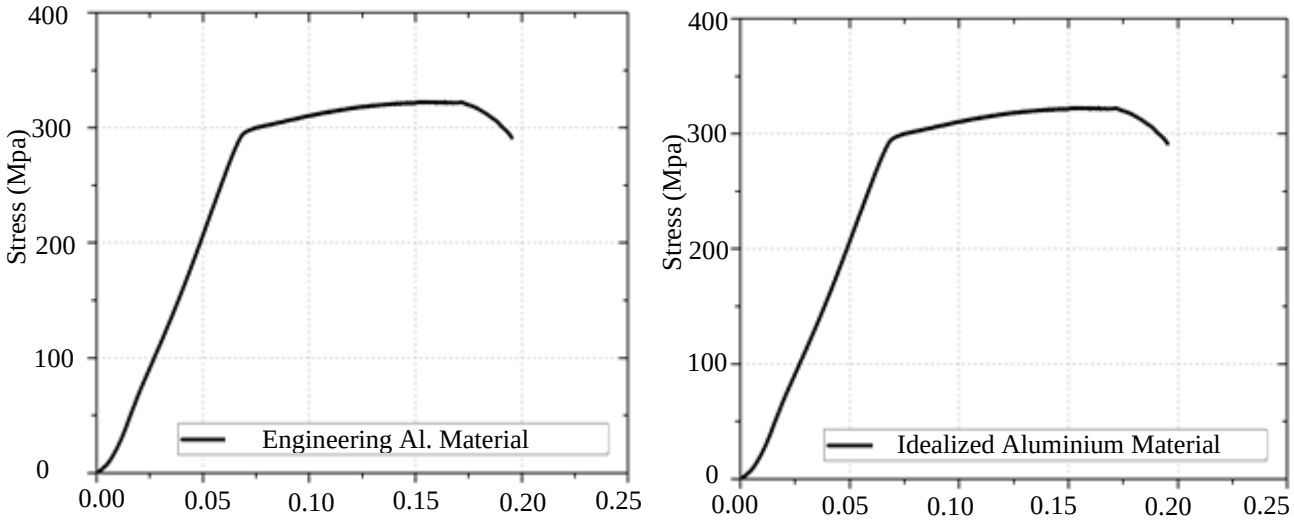

Fig. 2 Aluminium 6082-T6 material model for finite element analysis

Fig. 3 Aluminium joint strength testing in different orientations under bending loading

The FEM is not satisfactory for describing member buckling, and second-order effects resulting from structure geometric nonlinear influences can increase members' inner strength, leading to unfavourable states before complete structure buckling [29-31]. Overall, this study has important implications for the architecture and construction of monolithic dome structures in high-load applications. By improving our understanding of buckling behaviour and designing components to prevent it, we can create safer, more durable, and more efficient structures for various engineering applications.

Table 1. Summary of Aluminium 6082-T6 alloy material coupon test results

Coupon (N°)	Thickness (mm)	E_0 (Mpa)	$f_{0,1}$ (Mpa)	$f_{0,2}$ (Mpa)	f_u (Mpa)	$n=\ln 2/\ln(f_{0;2}/f_{0;1})$	$e = f_{0;2}/E_0$
1	10.00	69912	290	296	315	36.16	0.0042
2	10.00	69912	290	296	315	36.16	0.0042
3	10.00	69912	290	296	315	36.16	0.0042
4	10.00	69912	290	296	315	36.16	0.0042
5	10.00	69912	290	296	315	36.16	0.0042

Table 2. Geometric properties of kiewitt 8 domes

Structure Type	L (m)	f/L	n	θ_0 (deg.)	φ_0 (deg.)	f (m)	R (m)	l_0 (m)
K8	60	1/5	24	1.65	39.51	12.00	43.5	2.5
K8	60	1/8	24	1.12	26.96	7.50	63.75	2.5

2. Materials and Methods

2.1. Material Test and Joint Moment Capacity Testing

2.1.1. Aluminium 6082-T6 Alloy Testing

The Aluminium 6082-T6 alloy finished product sections shown in Figure 1 were used to create mate-rial test samples. These samples were acquired from the Aluminium body per the Chinese standard for Metal tensile specimen tests [32], and the resulting mechanical properties are recapitulated in Table 1. The resulting mechanical properties were used to develop an Aluminium material test model incorporated into the numerical program used to analyze the domes. The graphical portrayal of the model is presented in Figure 2.

2.1.2. Moment Capacity Testing in Aluminium Hexagonal Joints

The Aluminium hexagonal joints consider in this study are the same as the study in [33]. This study exclusively considers the T30. We extended our research to explore further T30-type joints. A set of six recently developed T30 Aluminium joints were subjected to testing. The joint was modelled and experimentally verified in both the bolt direction and orthogonal to the bolt direction, as shown in Figure 3 [33]. The mechanical capacity of the Aluminium connection model was obtained from experimental tests and integrated into the numerical program. Figure 4 displays the moment capacity curve for the T30 Aluminium Hexagonal joint for both the experimental and FEM results, which match well in both the bolt direction and orthogonal to the bolt direction. The T30-1 and T30-2 connection models were incorporated into the program as real constant *R1* and real constant *R2*, respectively, in the bolt direction and orthogonal to the bolt direction. The moment capacity was obtained from the mean values of all specimens and displayed in Figure 4.

2.2. Numerical Investigation of Dome Instability in Semi-Rigidly Jointed Structures

2.2.1. Geometric Description of the Studied Single Layer Kiewitt Domes

The research model studied in this article is single-layer Kiewitt 8 domes, as depicted in Figure 5. Table 2 illustrates the geometric aspects of the analyzed domes, where *n* represents the number of segments on the radial axis. The domes have fixed vertical boundaries at the base and are supported on a tension ring at the circumference. The span *L* and the rise/span ratio *f/L* are specified in Table 2, and the half-subtended angle θ_0 is calculated to represent the inclination of the roof for the members at the dome apex. The members are presumed to be made of Aluminium T6-6082, and the model considers tubular cross-sections. Structural characteristics of the examined model are enumerated in Table 2, including the radius of curvature, spans, and heights of the domes at the center. The members are semi-rigidly jointed at nodes, and their lengths on the rib lines l_0 are also specified in Table 2. The yield strength and Young's modulus of the Aluminium T6-6082 are presumed to be 296 MPa and E=69912.23 MPa, respectively. While the extent of the dome may affect its buckling behaviours, it is not considered significant in this study.

2.2.2. Features and Capabilities of BEAM189 Element

BEAM189 is a powerful tool for analyzing beam structures that are thin to moderately robust. It is derived from the Timoshenko [34] beam theory, which accounts for shear strain effects. This investigation's 3-D quadratic beam element permits unconstrained and constrained cross-sectional warping. Each node has six independent parameters, including movements in the three-dimensional coordinate system and rotations about those axes.

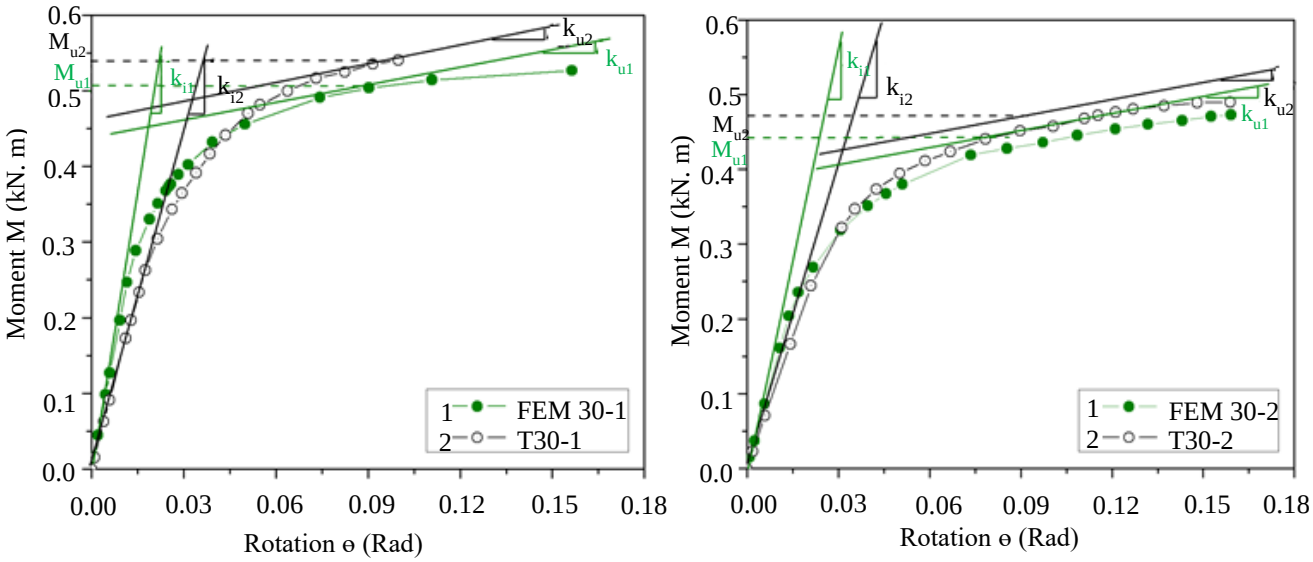

Fig. 4 Validating FEM results with test results for T30 aluminium hexagonal joint

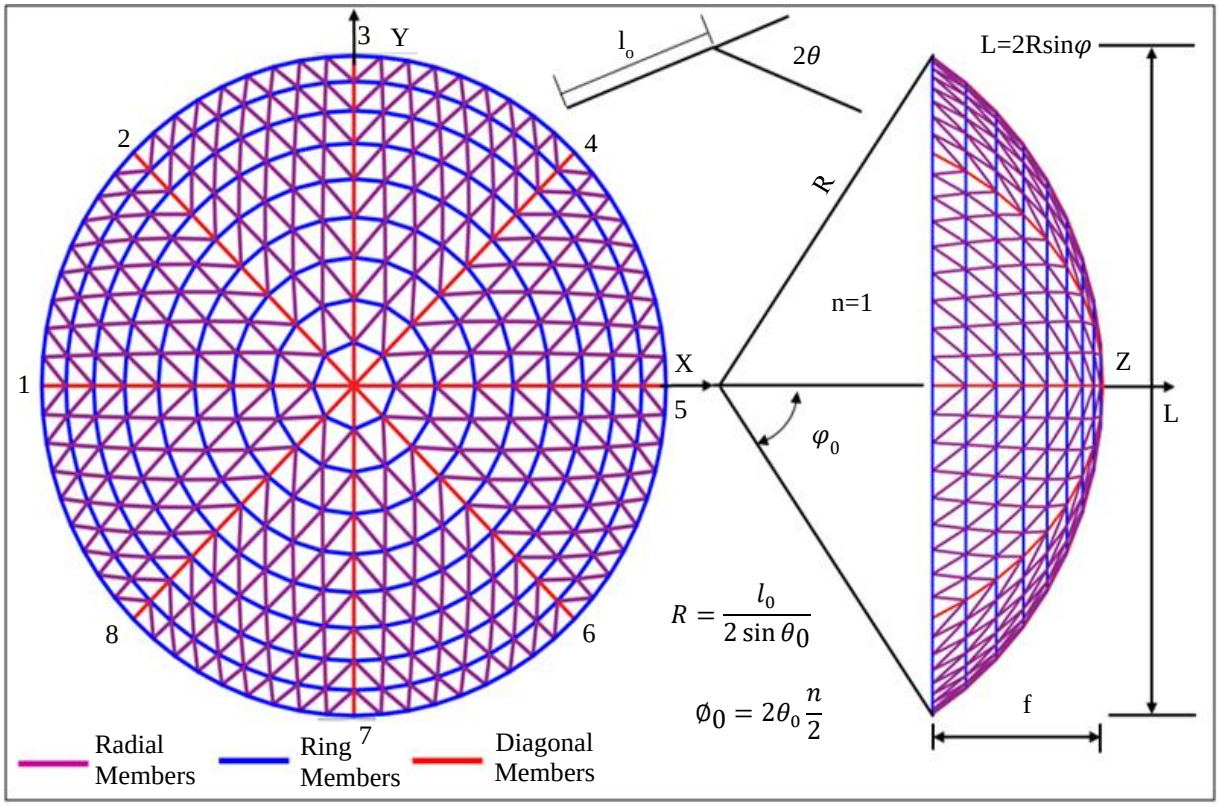

Fig. 5 Illustration of the kiewitt8 geodesic dome structure

If needed, there is an alternative seventh independent parameter for warping magnitude. The element is functional for linear, high rotation, and large-deformation nonlinear behaviour applications. Figure 6 illustrates BEAM189 Element's geometry. However, owing to the restrictions of the 1st-order shear hypothesis, it is only appropriate for evaluating structures of moderate to slender proportions.

2.2.3. Geometric Properties and Capabilities of COMBIN39 Element

COMBIN 39 is an element that exhibits nonlinear force-deflection characteristics. It applies to longitudinal and torsional loads in one-dimensional, two-dimensional, or three-dimensional cases. The longitudinal option has up to three independent parameters for movements in the Three-dimensional coordinate system at every vertex.

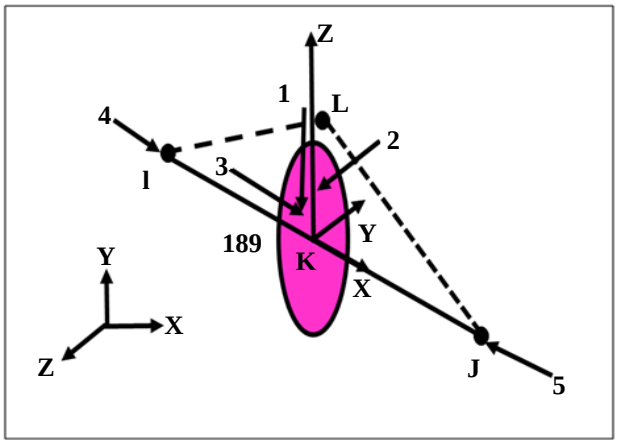

Fig. 6 BEAM189 geometric representation

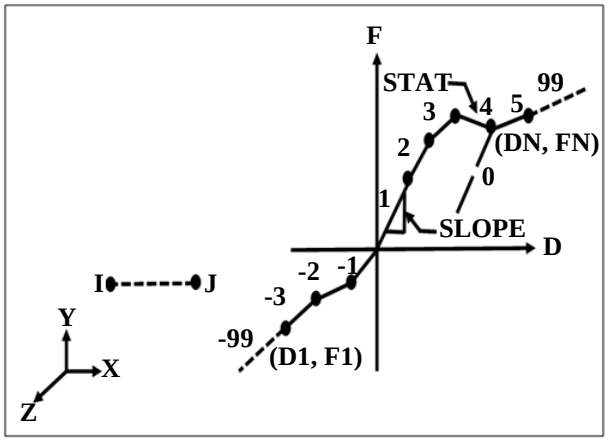

Fig. 7 COMBIN39 element geometry and construction illustration

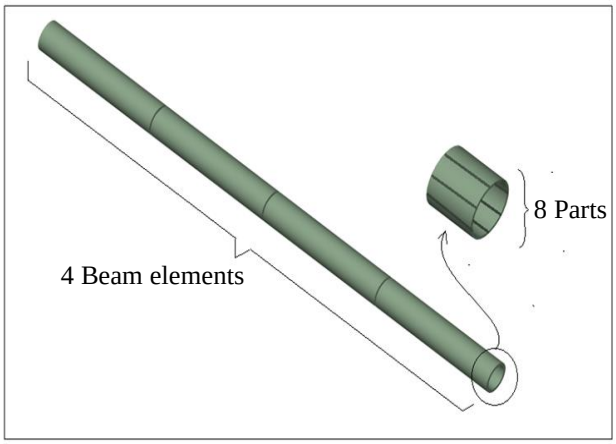

Fig. 8 4 BEAM189 element meshing model for tube members

In comparison, the torsional option has three independent parameters for rotations in nearly the three spatial dimensions.

The element can have a large displacement and two or three independent parameters at every vertex. The structural geometry, vertex locations, and geometric coordinates for this element are illustrated in Figure 7. It is characterized by two nodal points and a generalized force-deflection curve, where the points on the curve represent force or moment versus relative translation or rotation. The loads should be defined on a complete 360-degree basis for an asymmetric analysis.

2.2.4. Division and Meshing of Members in Dome Structures using Beam189 Element

The nodes connecting the members of each structure are presumed to have semirigid connections. The structure is rigidly fixed at the base and sustains a uniformly distributed vertical load.

The structures were modelled using ANSYS 15.5 Finite-Element software. A 3-D linear finite strain beam element using a mathematical model of beam theory [34] called Beam189 is utilized to model the members.

Each member is segmented into eight parts and meshed with four Beam189 elements, as displayed in Figure 8. Nonlinearities in geometry and material behaviour study (GMNA) is conducted [35] for each dome using Forde and Stiemer's proposed method [3]. Figure 8 illustrates the 4 BEAM189 element meshing model for tube members.

2.3. Buckling Curves of Kiewitt8 Members

2.3.1. K8 Domes Buckling Response

In this study, an established methodology widely employed by researchers involves investigating the load-deflection curve, commonly known as the nonlinear equilibrium path, at specific nodes. This approach offers valuable insights into structural behaviour, particularly regarding stability analysis and the influence of initial imperfections [25, 36-42]. The ANSYS software package facilitated this analysis due to its robust capabilities in simulating complex structural responses.

For each dome analytical model K8, an in-depth geometric and material nonlinear investigation (GMNA) was conducted. The GMNA method, initially proposed by Forde and Stiemer, was implemented to trace the nonlinear equilibrium trajectories [35,3] accurately. The resulting load-deflection graph, illustrated in Figure 9 for rigid and T30 Aluminium Connections, visually represents the structural response under various loading conditions. Additionally, the ultimate load values obtained from the analysis are summarized in Table 3, providing essential insights into the structural capacity and performance.

By employing this rigorous analysis methodology, valuable insights can be obtained regarding the structural behaviour and potential failure modes. The findings presented in this study contribute to a more profound comprehension of structural response and can inform future design considerations for similar structures.

2.3.2. Kiewitt 8 Column Buckling Strength

The strength and buckling behaviour of single-layer reticulated domes are significantly influenced by the rigidity and strength of their joints. Therefore, it is essential to conduct comprehensive investigations to determine the load-carrying capacities of such structures. The buckling strength of reticulated domes is evaluated using a design formula based on column strength curves. For K8 reticulated domes, the final strength is expressed in dimensionless parameters: the dimensionless final strength φ and the normalized slenderness ratio λ, which are analogous to those used for straight columns.

Through the application of GMNA analysis, the values of φ and λ are determined for specific members that have the most significant impact on the ultimate behaviour of the reticulated domes. Typically, this corresponds to the member experiencing the highest vertical position or displacement under the final load-carrying capacity of the dome. The calculations for φ and λ are performed using equation (1). For a more detailed understanding of the methodology employed, it is recommended to refer to Adeoti et al.'s work [33, 43-45].

$$\varphi = \left(\frac{1}{2\lambda^2}\right)\left[(1+\eta+\lambda^2) - \sqrt{(1+\eta+\lambda^2)^2 - 4\lambda^2}\right] \leq 1 \qquad (1)$$

Where: φ; λ and η are non-dimensional column strength, slenderness and imperfection parameters, respectively. α and λ0 parameters derived from numerical simulation results column curve fitting with various connection types. The strength curves for the dome structure are visually represented in Figures 10 and 11.The upcoming section will focus on dimensioning elements that encounter the simultaneous effects of bending and buckling forces.

3. Results and Discussion

Several buckling concepts require complete comprehension to understand the discussion about member dimensioning comprehensively. These concepts include the following: First order and second-order buckling, the P−δ effect or ε effect, the P−Δ effect, design optimization for components under axial forces, the buckling of structural elements (including the limit of validity of Euler's law), and the standardization of buckling curves.

3.1. Buckling Concept

3.1.1. Fundamental Concepts of Buckling

Buckling is an abrupt instability phenomenon that affects elements subjected to compression, partially or entirely. It is a frequently hidden issue that can suddenly occur within structural systems.

Table 3. K8 domes ultimate load (KN)

Structural Type	**K8 domes *f/L = 1/8***		**K8 domes *f/L = 1/5***	
Connection Type	Tube Section		Tube Section	
Rigid Joint	69.24	73.58	85.63	85.91
Al. HBC Joint	49.88	51.49	73.19	73.58

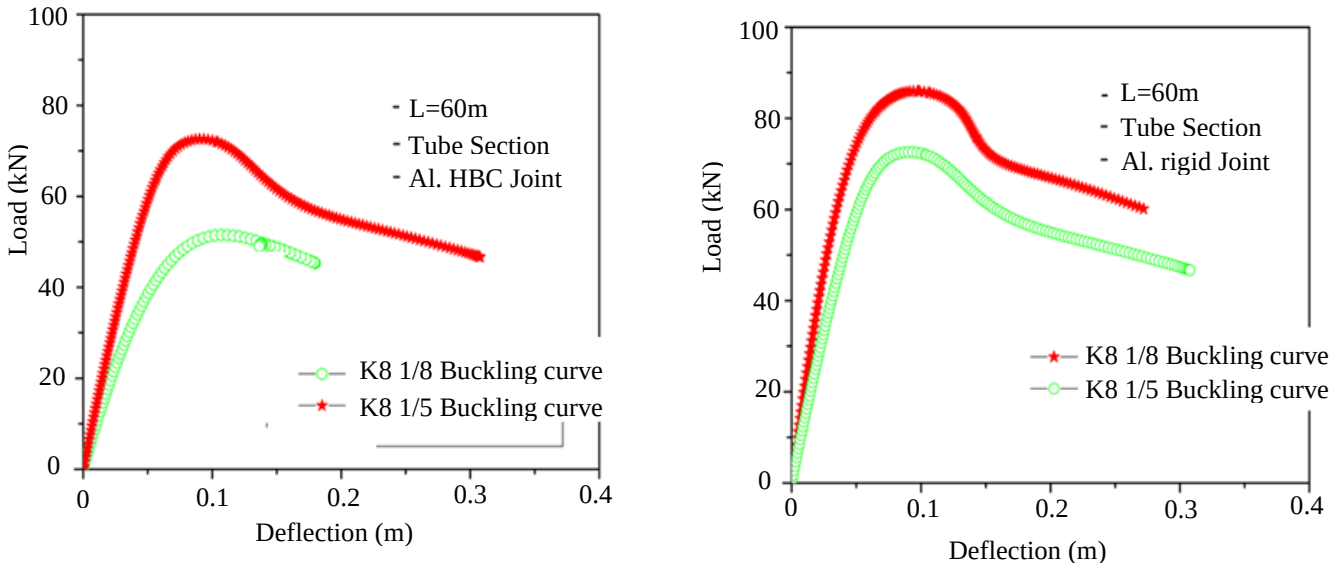

Fig. 9 K8 buckling graph with rigid and Al. T30 connection type

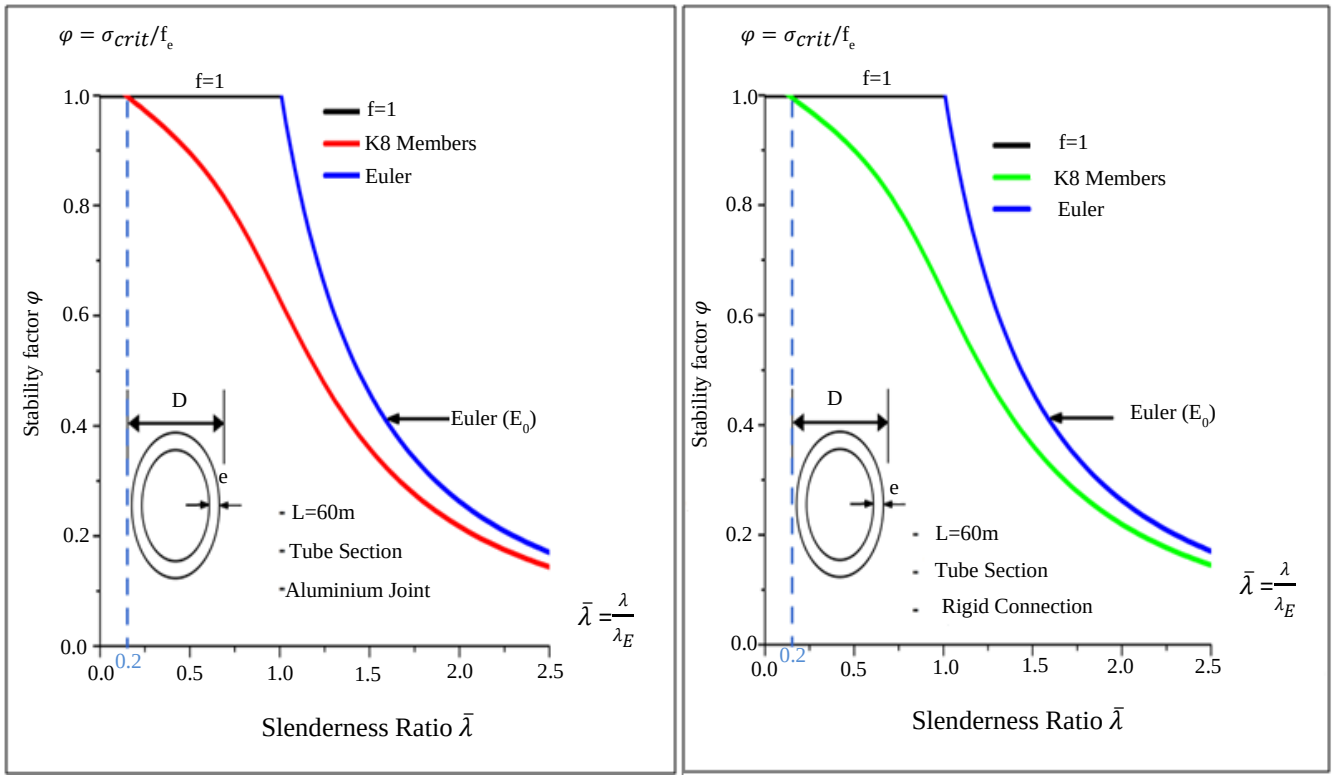

Fig. 10 Kiewitt8 dome strength curves with rigid joint and Aluminium T30 joint

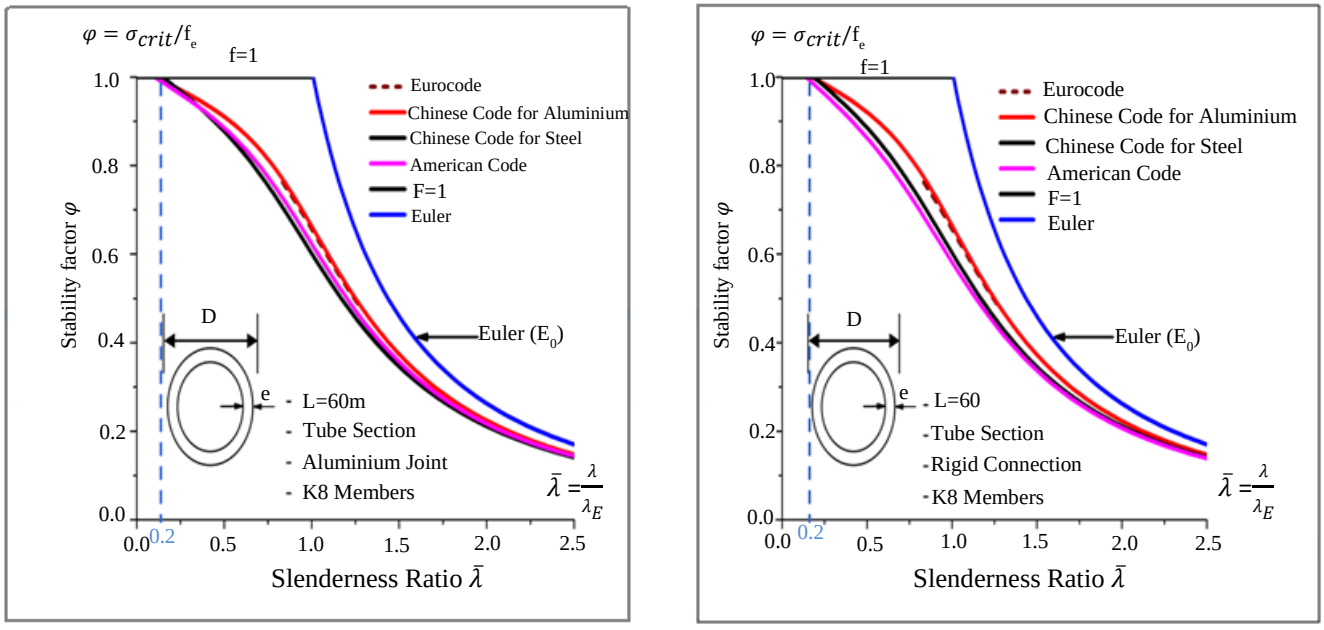

Fig. 11 Kiewitt8 dome strength curves with rigid joint and Aluminium T30 joint express in various codes

Hence, it is essential to proactively prevent buckling to safeguard the structural integrity and the well-being of occupants or users. Some civil engineering structures, such as sailboat masts, are particularly susceptible to buckling and should be carefully accounted for. Buckling is often defined as a second-order effect with diverging characteristics and can be triggered by manufacturing imperfections or disturbances. Indeed, even with impeccable manufacturing, no element can be perfectly straight. At the microscopic level, some form of imperfection will always be present.

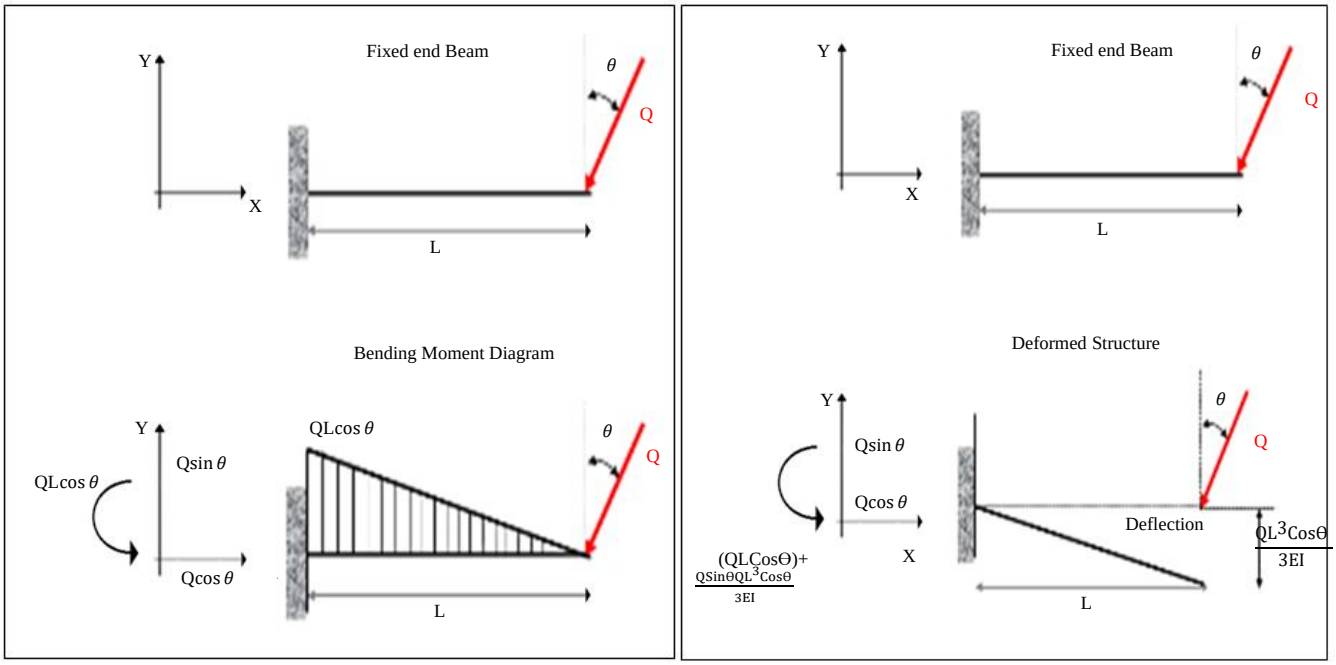

Fig. 12 Fixed-end beam analysis

These imperfections can arise from the tiniest deviations in the compressive force relative to the average fibre (buckling due to imperfection) or the combined implementation of a bending moment on the element (known as buckling due to disturbance).

Consequently, the normal force F always acts with some degree of eccentricity e0, no matter how small, resulting in a parasitic bending moment $M_0 = Fe_0$. This moment induces curvature, exacerbating the eccentricity of the applied compressive force, leading to a cascade of increasing deformations. This progressive amplification of deformations is commonly known as buckling by divergence [46-47].

3.1.2. First Order, Second Order, P−δ Effect or ε Effect, P−Δ Effect

Let's consider a structure initially not subjected to loads with a defined geometry. When a load is exerted on this structure, it undergoes deformation and reaches a new equilibrium state with a different geometric configuration than its original form. Although the consequent deformations are generally small and barely perceptible to the naked eye.

Considering the deformed shape to analyze the deformed structure accurately and derive equilibrium equations for statics to calculate internal forces would be imperative.

However, this is impractical because assessing the changed shape requires knowledge of the internal forces, which can only be initially determined based on assuming equilibrium in the undeformed structure.

This initial calculation, commonly known as a first-order calculation, is widely used in most cases. Let us take a fixed-end beam with inertia moment *I* and length *L*, where a force *Q* is applied at an angle θ: If we perform a first-order calculation, we assume that the beam remains in its original, undeformed geometry. This allows us to find the support responses and the associated flexural moment diagram, as depicted in Figure 12.

In reality, the beam experiences deflection, and the deflection at the end is defined by the mathematical *equation* $\delta=QL^3cos\theta/3EI$, as depicted in Figure 12. Reevaluating the force equilibrium based on this deformed structure, the horizontal projection of *Q* introduces a non-zero lever arm regarding the fixed end, causing the initial bending moment to be increased by a multiple of $1+QL^2sin\theta/3EI$.

This subsequent analysis is a second-order analysis and can be extended indefinitely by considering incremental deflections and higher orders. When these successive deflections diverge, the phenomenon of buckling arises.

Second Order, Third Order, ..., Second Order

The physical understanding of buckling has demonstrated that it arises when there is a divergence among successive deflections of varying orders, including first, second, third, and beyond. However, it is significant to mention that this interpretation is purely mathematical. In reality, the combined phenomena of successive orders, ranging from two to infinity, can be encapsulated as a unified effect known as the second-order effect within the context of this article.

P-Delta Effect (P - Δ)

Let us clarify from the start that the *P*-Δ effect should not be confused with the *P*-*δ* effect. The first is linked to the overall behaviour of a structure, while the latter concerns the individual behaviour of an element. In a structural framework, the inherent lack of perfect verticality leads to gravitational loads being applied to columns with some eccentricity. As a result, additional bending moments are induced, supplementing the forces calculated in the first-order analysis.

If the structure is flexible or poorly braced, these effects can be amplified and further compounded by horizontal loads, often caused by wind acting on the facades. This phenomenon, known as the *P*-Δ effect, is directly correlated with the deformed state of the structure. It can be justified by amplifying the first-order effects to a certain extent or by conducting a second-order analysis that explicitly considers the P-Δ effect through computational software [46-50].

*P-Delta Effect (*P-δ*) or ε Effect*

Let us begin by emphasizing that it is essential to distinguish between the *P*-Δ effect and the *P*-*δ* effect. The earlier is aligned with the behaviour of a structure as a whole, while the latter relates to the individual behaviour of an element. Scientific research has proven that even a minimal imperfection in the straightness of an element, when subjected to a compressive normal force *F*, gives rise to second-order moments that are not directly correlated with the applied load. Instead, these moments amplify the maximum first-order moment Fe_0 by a factor calculated as:

$$\mu = \frac{1}{\frac{1-F}{F_{crit}}} \quad (2)$$

Here, F_{crit} represents the Euler critical charge of the element. Likewise, when an element experiences combined bending, with an average force *F* and a bending moment *M* acting on it, the first-order bending moment *M* is amplified by the same corrective factor 1/(1-*F/Fcrit*). This phenomenon is commonly known as the *P*-*δ* effect.

Regarding Element Design, Two Scenarios can be considered

- With regard to pure compression, one can apply analytical buckling formulas that implicitly account for this effect.
- In situations involving combined bending, it becomes necessary to consider the buckling formulas and multiply the first-order bending moment by the corrective factor 1/(1-*F/Fcrit*).

When It Comes to Designing the Overall Structure

- The amplification effect of $P-\delta$ leads to a perceived reduction in the flexural stiffness of the element. Consequently, this effect can potentially provoke the transfer of loads within the structure, especially if it is statically indeterminate [35,46,49-50]

Summary

The second order can arise from an imperfection, such as a manufacturing defect or a disturbance, such as a side wind, as depicted in Figure 13.

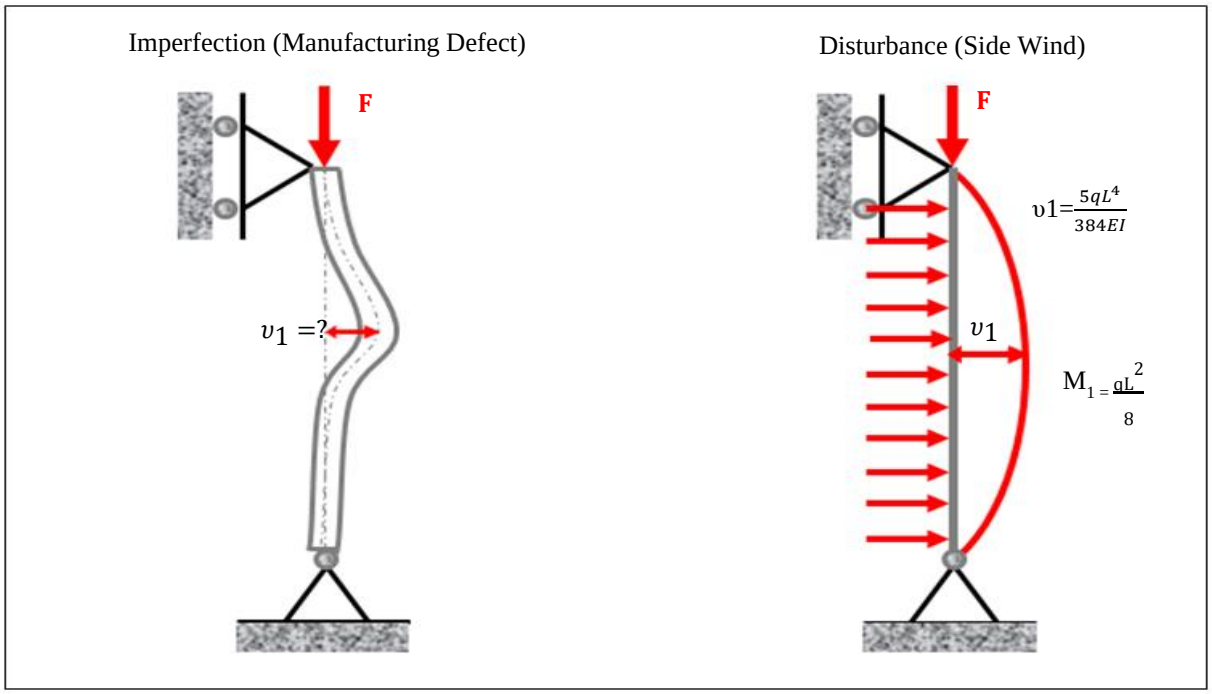

Fig. 13 Origin of second-order buckling

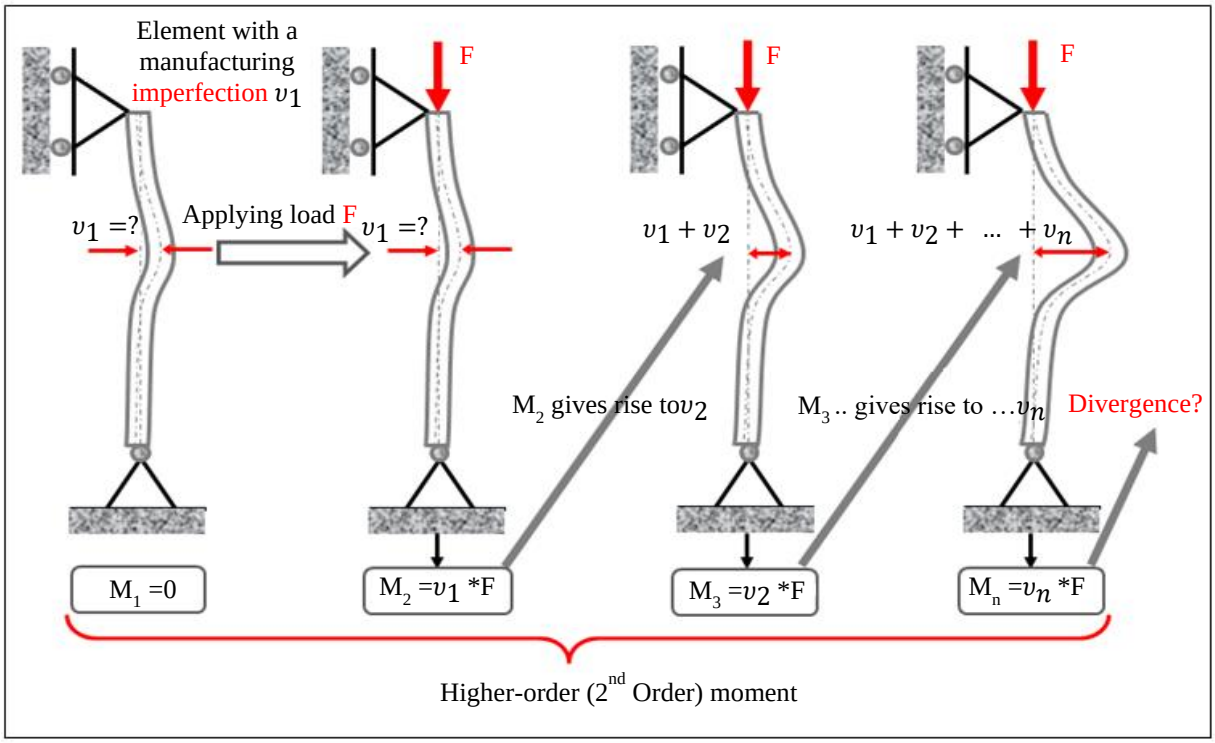

Fig. 14 Second-order buckling analysis: element with manufacturing imperfection

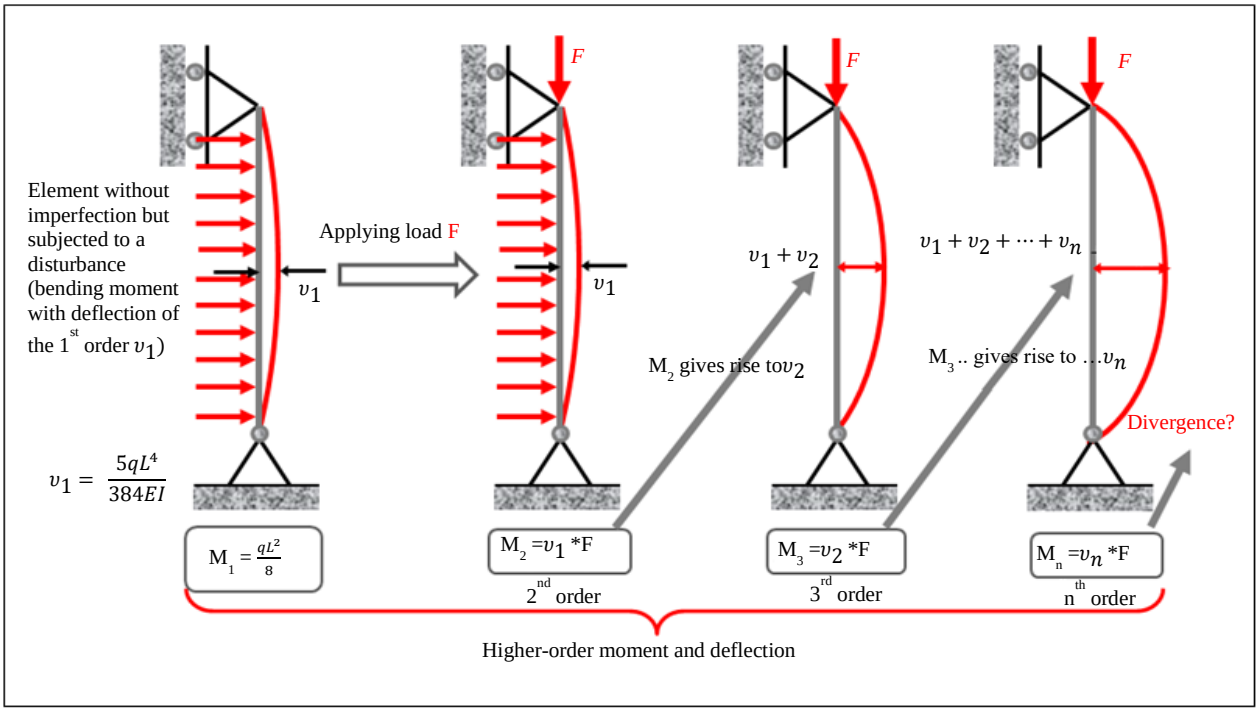

Fig. 15 Second-order buckling analysis: element subjected to disturbance

Compressing the element in either situation will generate unexpected moments with a magnitude equal to Fv_1. The first intuitive approach to second-order effects is illustrated in Figure 14, where an element with an imperfection *v1* is shown. Figure 15 presents the second intuitive approach to second-order effects, depicting an element without imperfection but subjected to a disturbance (a bending moment with a first-order deflection, v_1).

From these observations, we conclude that second-order effects occur in two ways: either due to a manufacturing defect (imperfection) or a bending deformation caused by a disturbance (such as lateral wind on a compressed column). These effects always arise when a flexural moment is combined with a normal force. The ratio M_n/M_1 is recognized as the amplification factor equal to ν_n/ν_1. Buckling is thus a diverging second order phenomenon, as depicted in Figure 16.

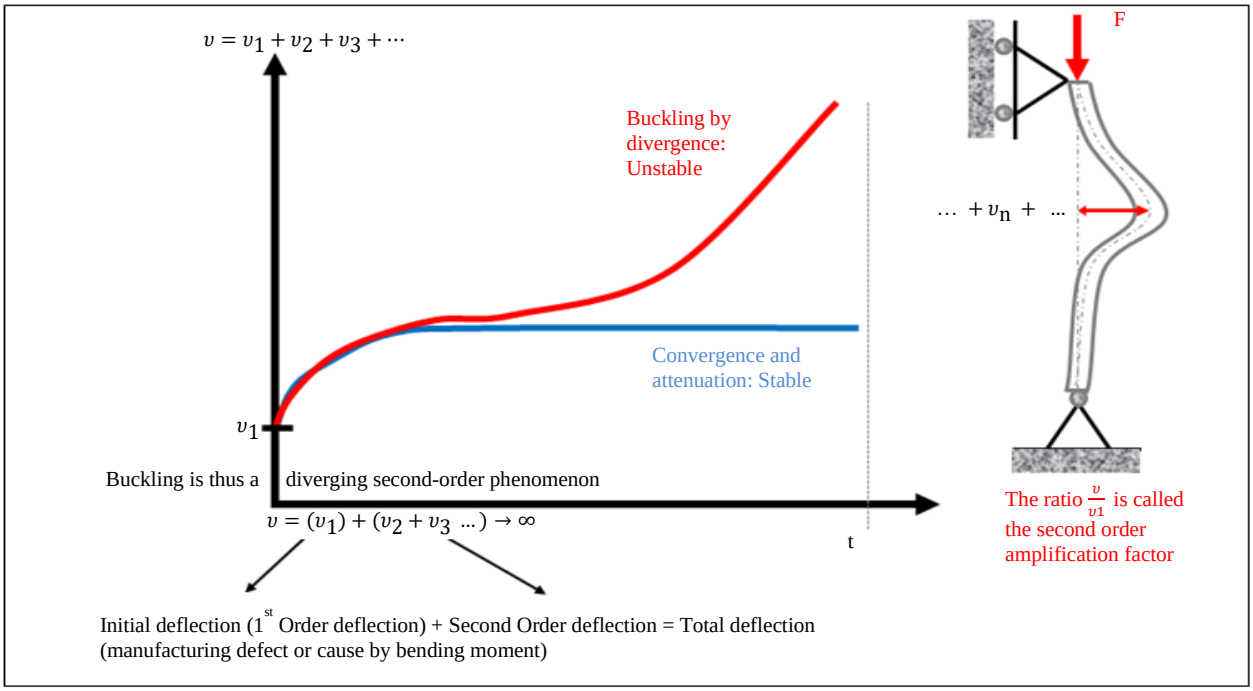

Fig. 16 Buckling with diverging second-order phenomenon

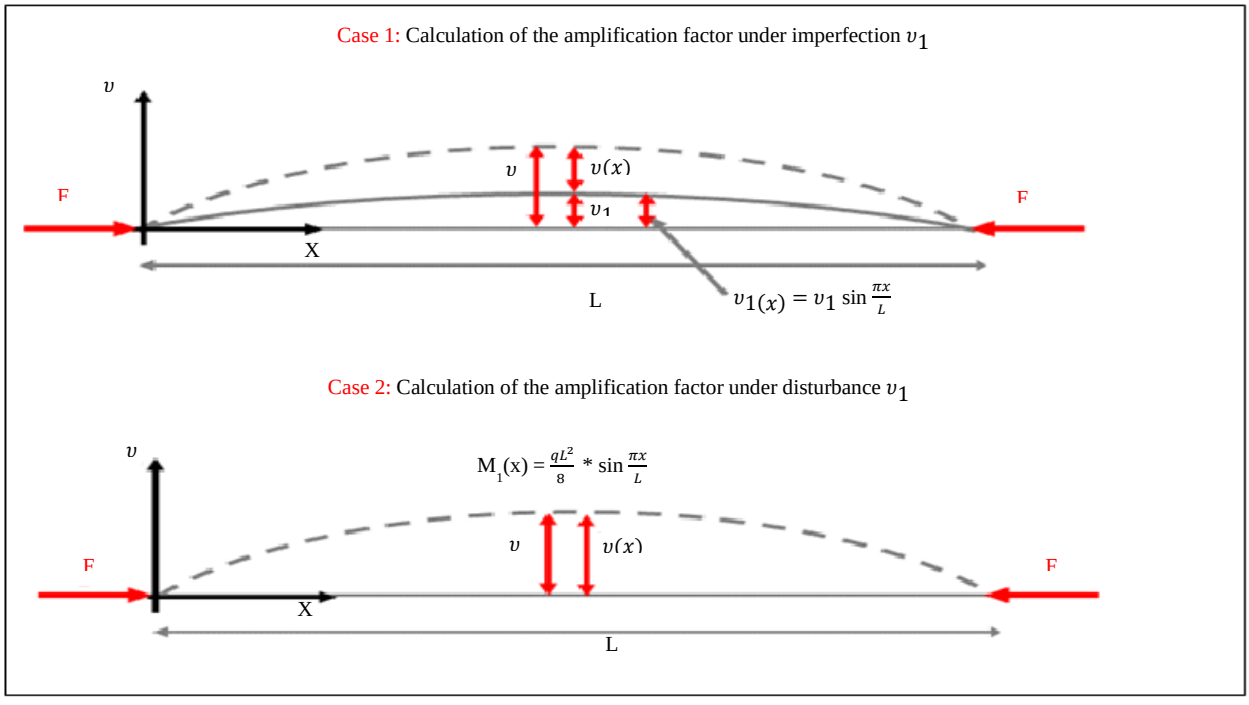

Fig. 17 Second-order buckling analysis

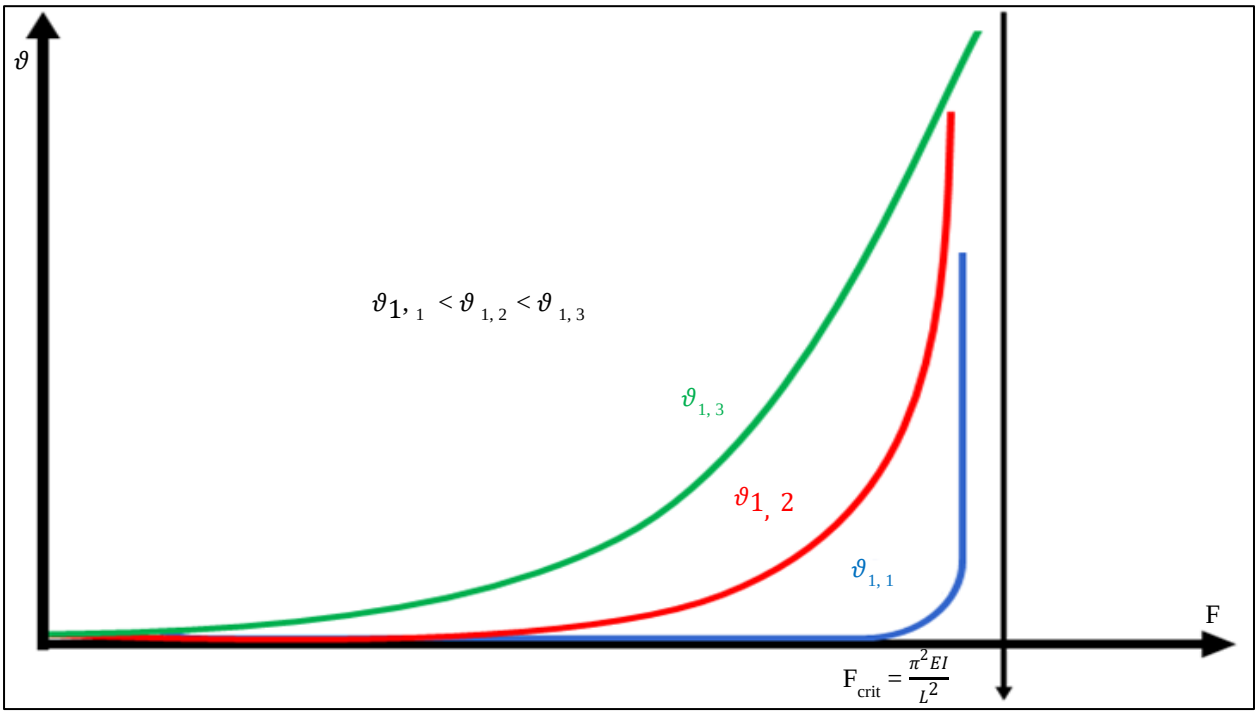

Fig. 18 Influence of defects on the response of euler critical load

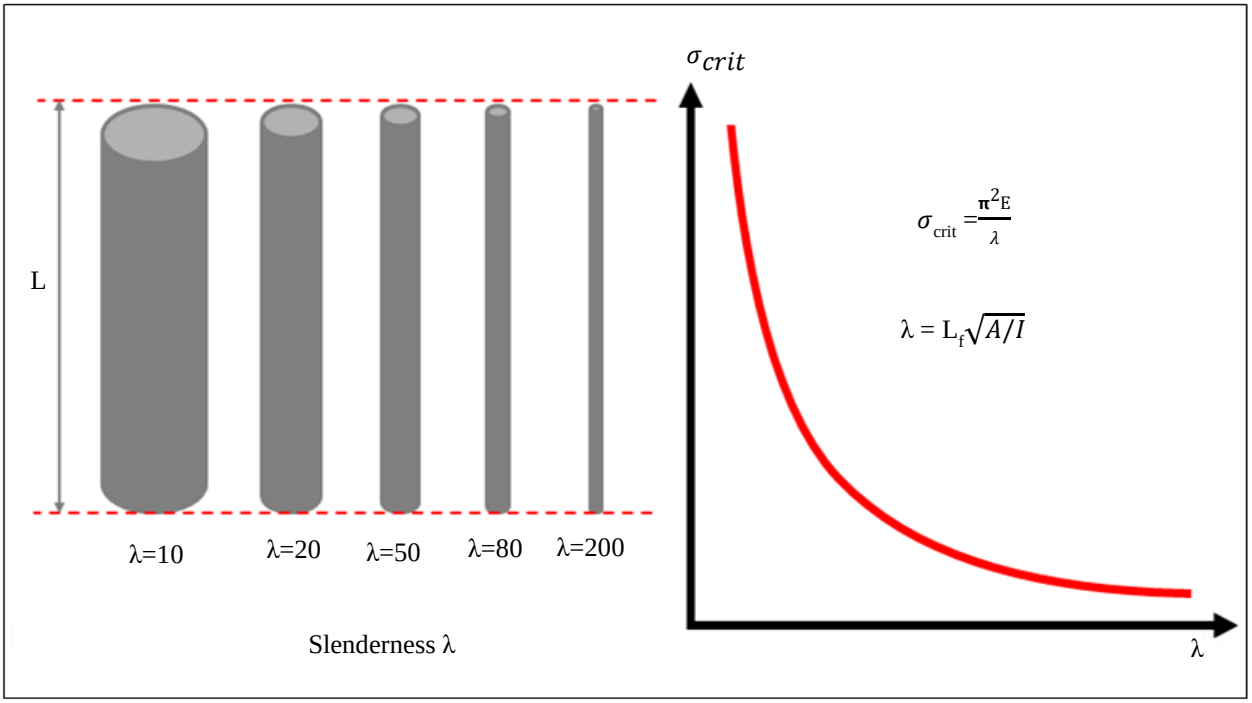

Fig. 19 Slenderness and buckling sensitivity

$$\left(\frac{1}{1-F/F_{crit}}\right)\left(\frac{qL^2}{8}\right) \quad (3)$$

$$\left(\frac{1}{1-F/F_{crit}}\right)\left(\frac{5qL^4}{348EI}\right) \quad (4)$$

The second-order effect increases the initial bending moment M_1 by amplifying $1/(1–F/F_{crit})$, where $F_{crit}=\pi^2EI/L^2$. Consequently, Equations (3) and (4) determine the total bending moment and deflection. This occurrence is witnessed in the given scenario of the uniformly loaded beam, where a sinusoidal shape approximates the parabolic

moment distribution. It is essential to highlight that this finding holds implications for a broad spectrum of bending scenarios, suggesting its potential for generalization. (Figure 17), the refinement scale can vary depending on the specific conditions, resulting in a spectrum of precision with differing degrees.

$$\left(\frac{1}{1-F/F_{crit}}\right)M_1(x) \tag{5}$$

$$F = F_{crit} = \frac{\pi^2 EI}{L^2} \tag{6}$$

Consequently, the amplification factor is determined to be Equations (5). We can derive from equation (5) that the moment tends towards infinity when *F* is equation (6). This critical value is identified as Euler critical charge. The Euler critical load remains independent of the extent of the production imperfection ν1 and the first-order bending moment, representing the disturbance pictured in Figure 18.

3.1.3. Engineering Design Optimization and Improvement

Based on the graphical representation of Euler's formula in Figure 19, It is evident that with an augmentation in the slenderness ratio, it can be observed that the likelihood of buckling occurring under low-stress conditions also increases. A summarized compilation of the sensitivity to buckling to different slenderness ratios is presented in Table 4. From the data in this table, it can be inferred that slenderness ratios within the spectrum of 0 to 20 exhibit negligible sensitivity to buckling.

Table 4. Slenderness and buckling sensitivity

Slenderness λ	Buckling Sensitivity
0 − 20	None
20 − 50	Low to Moderate
50 − 80	High
80 − 200	Extremely High
≥ 200	Refrain

The sensitivity of slenderness ratios between 20 and 50 is low to moderate. When the slenderness ratios fall within the range of 50 to 80, the sensitivity is classified as high, and ratios between 80 and 200 are considered extremely high. To ensure structural integrity, it is advisable to refrain from constructing elements with slenderness ratios exceeding 200. Elements with such high ratios are inherently flawed, rendering Euler's law less representative. Furthermore, the geometry of these elements does not facilitate precise and secure application of Euler's law.

3.1.4. Design Optimization for Components under Axial Forces

Upon investigating the bending phenomenon, it becomes apparent that elements subjected to such forces consistently necessitate substantial moments of inertia within their cross-sectional profiles. A more excellent moment of inertia contributes to lower bending stresses, leading to diminished deformations. This correlation finds affirmation in Euler's law. A more excellent moment of inertia aligns with a higher critical load requirement. In simpler terms, as the section size increases, a higher compressive force is needed to induce buckling.

Referencing Figure 20, it is observed that material usage can be optimised by systematically removing material from sections centroid while maintaining consistent moment of inertia, length, and Euler's critical load. Let us denote the area and inertial moment of the solid section as A_0 and I_0, respectively. The solid section exhibits a thickness-to-outer-diameter ratio of 1/2.

Table 5. Various elements details

e⁄ϕ0	ϕ0	A0	λ0
0.5	100	100	100
e⁄ϕ	ϕ	A	λ
0.2	104	69	83
0.1	114	47	68
0.05	131	32	57
0.02	161	20	45

Refer to Table 5 for specific details concerning various elements. The inertial moment for a hollow section can be determined using Equation (9):

$$A_0 = \frac{\pi {\phi_0}^2}{4} \tag{7}$$

$$I_0 = \frac{\pi {\phi_0}^4}{64} \tag{8}$$

$$I = \frac{\pi {\phi_0}^4}{64}\left(1 - \left(1 - \frac{2e}{\phi}\right)^4\right) = C^{ste} = I_0 \tag{9}$$

$$\frac{\phi}{\phi_0} = \left(1 - \left(1 - \frac{2e}{\phi}\right)^4\right)^{-1/4} \tag{10}$$

$$A = \frac{\pi \phi^2}{4}\left(1 - \left(1 - \frac{2e}{\phi}\right)^2\right) \tag{11}$$

$$A = \frac{\pi \phi_0^{\,2}}{4} \frac{1-\left(1-\frac{2e}{\phi}\right)^2}{\sqrt{1-\left(1-\frac{2e}{\phi}\right)^4}} \quad (12)$$

$$A = A_0 \frac{1-\left(1-\frac{2e}{\phi}\right)^2}{\sqrt{1-\left(1-\frac{2e}{\phi}\right)^4}} \quad (13)$$

When comparing the amount of material present in consecutive hollow sections, which reflects the cross-sectional area, it is evident from equation (10) that the ratio A/A_0 between a hollow section and a solid section with an equivalent moment of inertia can be expressed by equation (13).

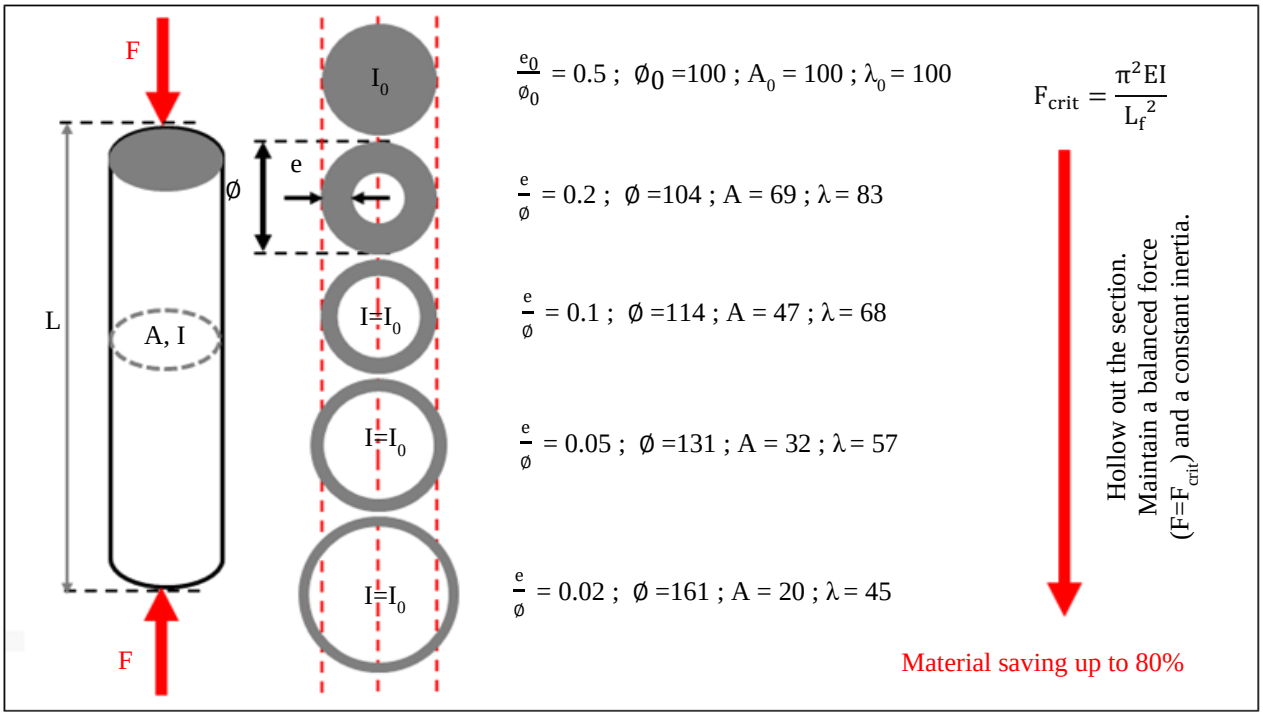

Fig. 20 The influence of the e/φ ratio on the dimensions of the section and the value of section A is examined, assuming the use of homogeneous material with identical I and F values

This ratio is established by the relationship between *e/φ*, representing the wall dimension and the outer diameter. Notably, the extent of the diameter of the hollow section is 60% larger, while the area is only one-fifth of the solid section area. To summarize, two approaches can be adopted to lessen the impact of buckling and achieve material efficiency.

The first approach involves increasing the inertial moment by displacing material away from the centroid, which can be accomplished by hollowing out the section. The second approach focuses on reducing the buckling length, a critical factor in Euler's law, by incorporating appropriate supports at the ends and along the dimension of the element length.

3.1.5. Buckling of Structural Elements: Limit of Validity of Euler's Law

Euler's law overlooks the material's yield strength, denoted as f_e, and requires adjustment when dealing with small slenderness ratios. This is because Euler's law allows for the possibility of infinite normal stresses in such cases. The critical slenderness ratio, represented by λ_E, marks the point beyond which Euler's law no longer holds.

$$\sigma_{crit} = \frac{\pi^2 E}{\lambda^2} \quad (14)$$

$$\sigma_{crit} = \frac{\pi^2 E}{\lambda^2} \geq f_e \quad (15)$$

$$\lambda_E = \pi \sqrt{\frac{E}{f_e}} \quad (16)$$

$$\lambda = l_f \sqrt{\frac{A}{I}} \quad (17)$$

When examining Equation (14) and carefully studying the graph in Figure 21, it becomes apparent that minimal slenderness ratios can lead to material stress reaching infinite values.

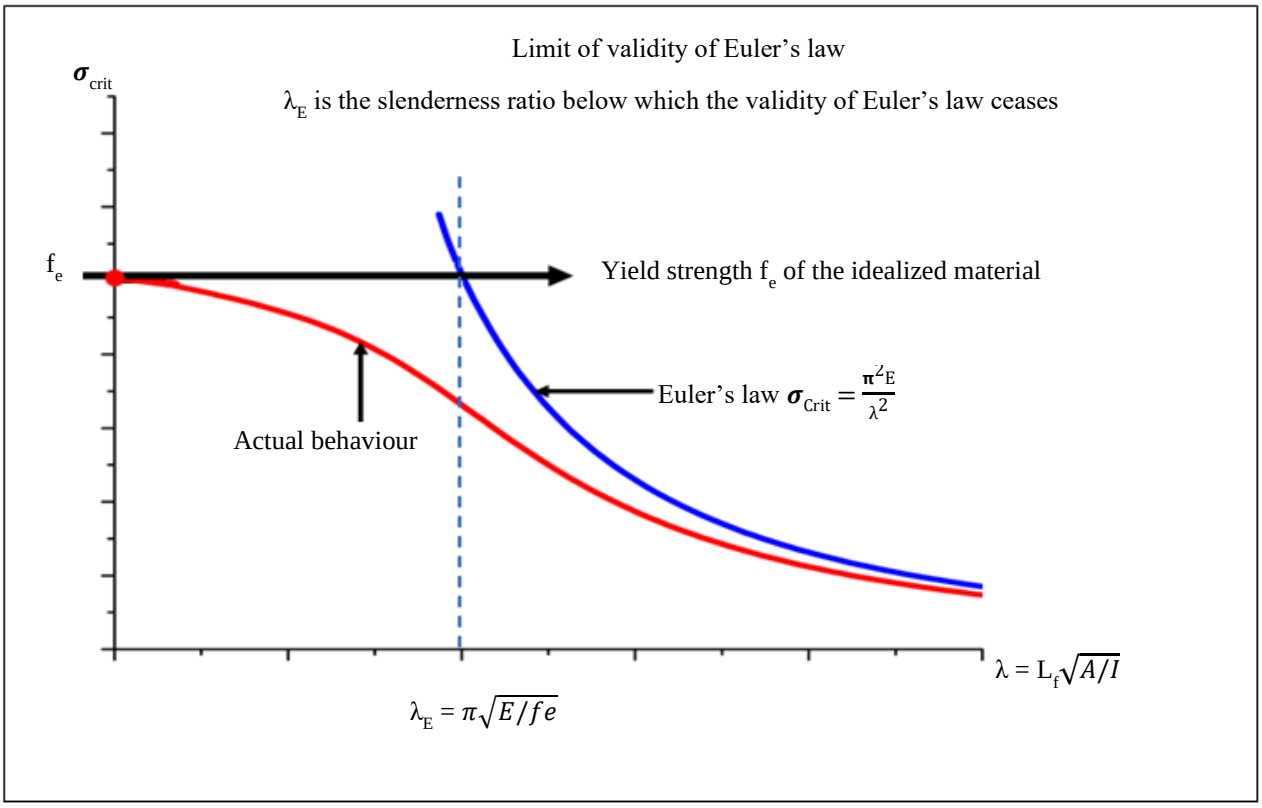

Fig. 21 Limit of validity of euler's law

This contradicts the inherent nature of materials, which possess defined yield strength, denoted as f_e. To address this issue, the curve coloured in red in Figure 21 presents the permissible stress values in a compressed element correlated with the slenderness ratio, ensuring that the material stays within the prescribed limits of its yield strength f_e. According to this curve, the material can be stressed up to its yield strength fe for compressed elements with small slenderness ratios approaching zero.

However, with the rise in the slenderness ratio, a need arises to diminish the stress exerted on the element gradually. As the slenderness ratio deviates from zero, it is essential to ensure that the stress within the element remains below the stress level present in the absence of buckling susceptibility—this sensitivity to buckling results in suboptimal material utilization. Increasing the element's size to maintain the stress below the elastic limit for a given load becomes necessary.

3.1.6. Standardization of Buckling Curves

Standardization of buckling curves is a critical process in scientific research. It establishes a consistent framework for investigating the response of structural elements to compressive forces. By analyzing data and identifying patterns, researchers can compare and predict the buckling behaviour of different structures. This leads to safer design practices and a deeper understanding of structural integrity. Standardization plays a pivotal role in enhancing the credibility of research findings and optimizing the efficiency of structural designs. Figure 22 depicts a typical standardized buckling curve.

$$\frac{\sigma_{crit}}{f_e} = \frac{\pi^2 E}{\lambda^2 f_e} = \frac{\left(\pi\sqrt{\frac{E}{f_e}}\right)^2}{\lambda^2} = \frac{{\lambda_E}^2}{\lambda} = \frac{1}{\bar{\lambda}^2} \qquad (18)$$

With:

$$\lambda = l_f\sqrt{\frac{A}{I}} \;\; ; \quad \lambda_E = \pi\sqrt{\frac{E}{f_e}} \;\; ; \; \bar{\lambda} = \frac{\lambda}{\lambda_E}$$

We can obtain valuable insights by analyzing standardized buckling curves with Euler's curve and yield strength. Euler's curve represents the critical load at which buckling occurs, while the yield strength provides information about the material's durability.

Comparing the standardized curves to Euler's curve allows us to assess the stability and safety margins of the structures. By examining the points of intersection of the curves or where they deviate from each other, we can understand how material properties and configurations influence buckling behaviour.

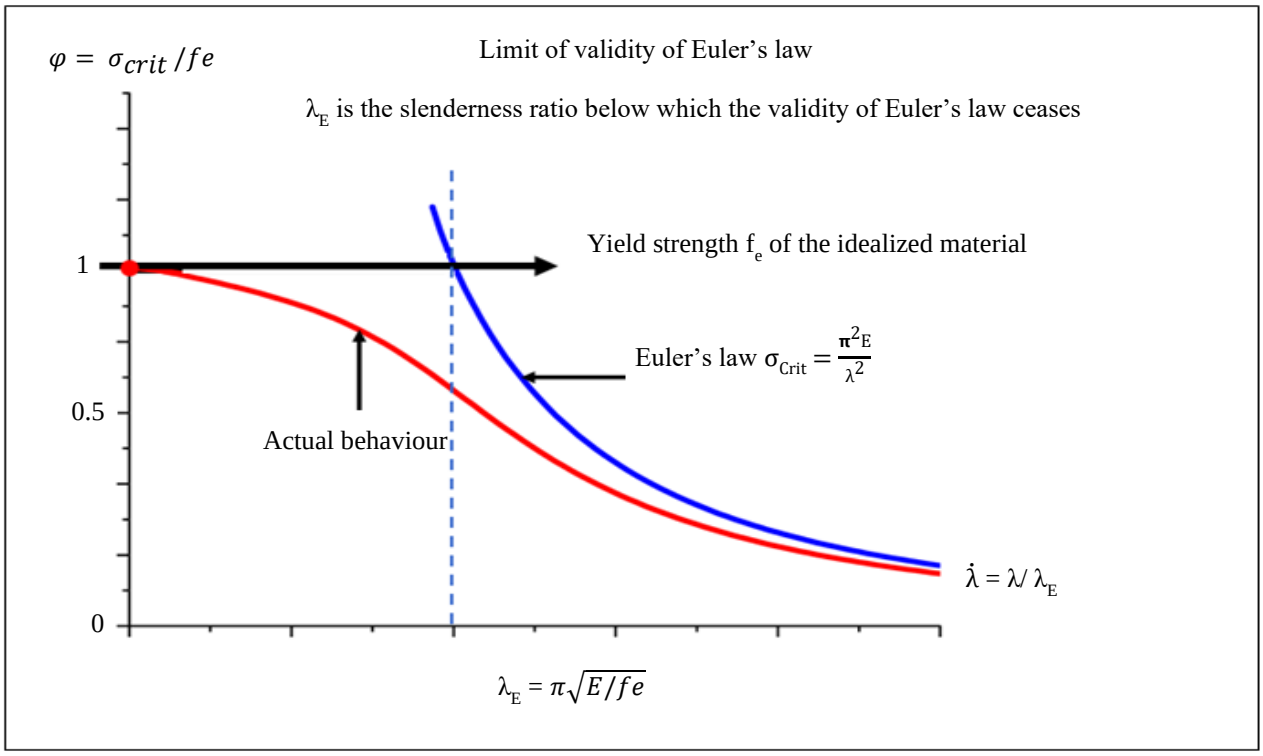

Fig. 22 Normalized buckling curves

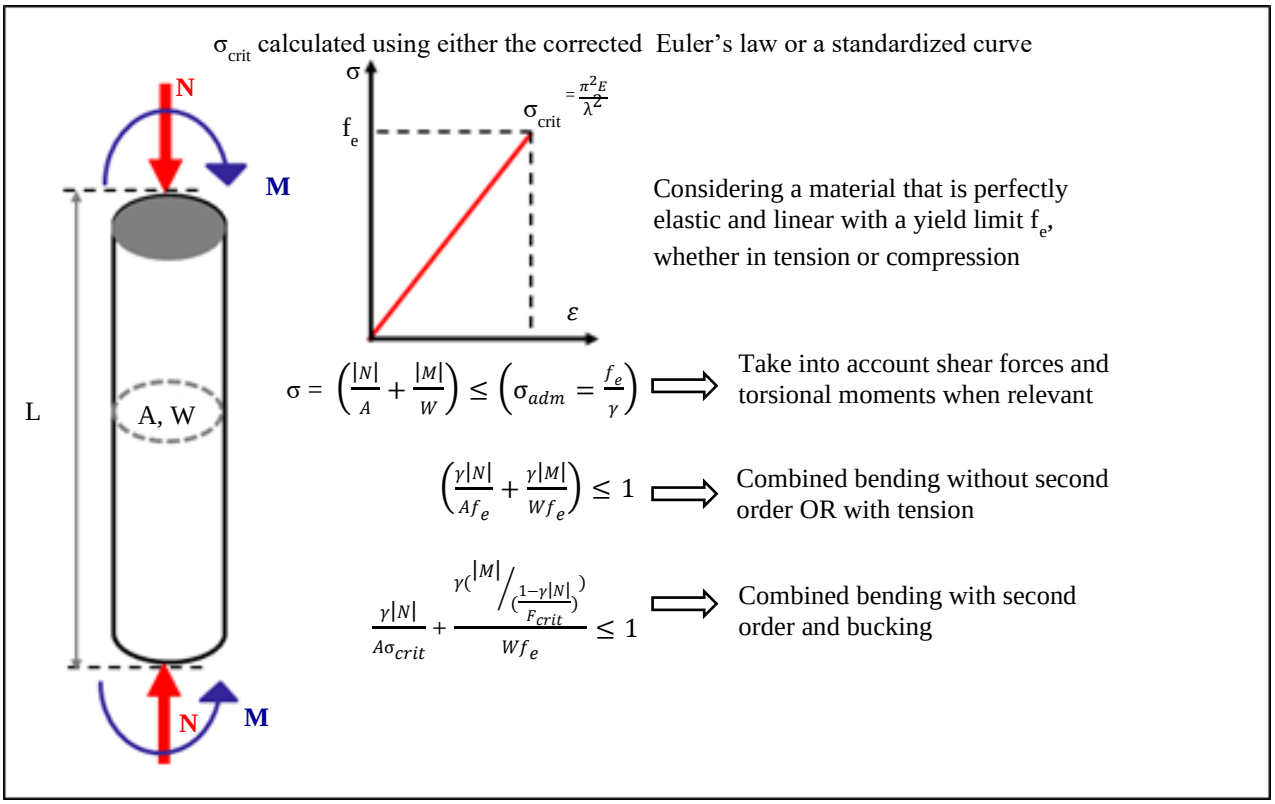

Fig. 23 Combined bending and buckling dimensioning

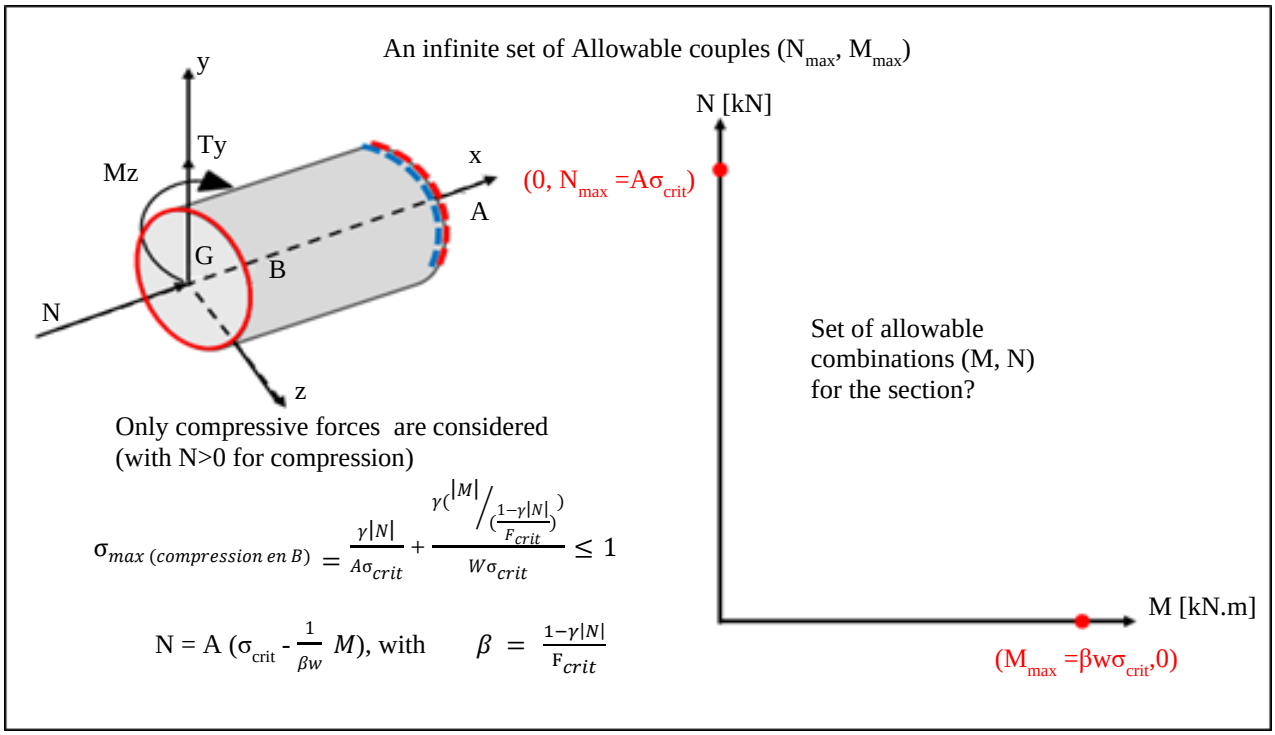

Fig. 24 An infinite set of allowable couples (N_{max}, M_{max})

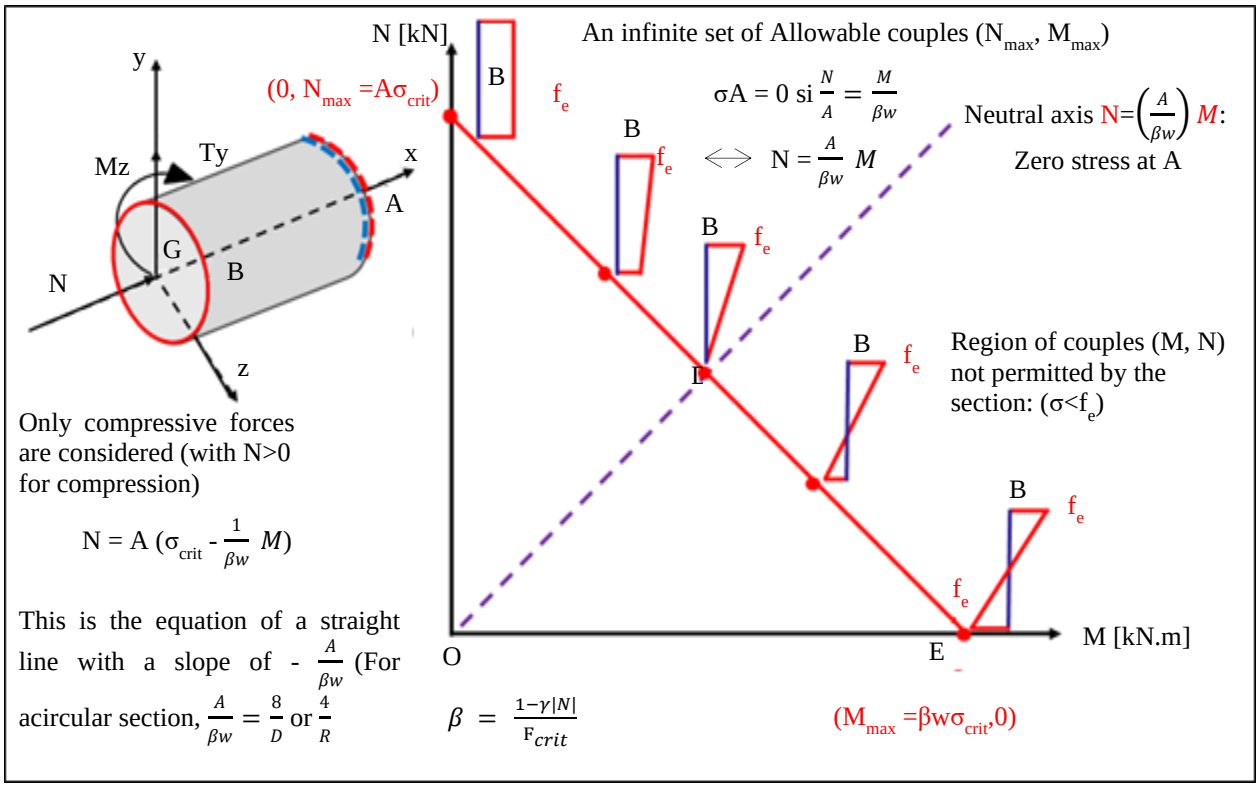

Fig. 25 An infinite set of allowable couples (N_{max}, M_{max}) analysis

These findings are essential in guiding design decisions by identifying potential failures. Analysing standardized buckling curves, Euler's curve and yield strength enhances our understanding of structural stability. This understanding plays a pivotal role in guaranteeing the security and reliability of engineering designs.

3.2. Discussion on Dimensioning of Elements Facing the Combined Influence of Bending and Buckling Forces

If we neglect both the secondary effects (moment amplification) and the susceptibility to buckling (effect on axial compression force *N*), we focus solely on examining the local behaviour within the sections. In such cases, the following inequalities hold:

$$\sigma = \frac{|N|}{A} + \frac{|M|}{w} \leq \frac{f_e}{\gamma} \tag{19}$$

$$\sigma = \frac{\gamma|N|}{Af_e} + \frac{\gamma|M|}{Wf_e} \leq 1 \tag{20}$$

Additionally, it is essential to consider incorporating shear stress and torsional moment whenever applicable. The expression $\gamma|N|/Af_e+\gamma|M|/Wf_e$) represents a section's utilisation ratio. Exceeding a utilization ratio of 1 indicates that the section has surpassed its failure state, while a utilization ratio of 1 implies that the section is appropriately sized. Conversely, a utilization ratio below 1 suggests that the section is oversized, providing a significant safety margin and resulting in material wastage.

Notably, this criterion applies explicitly to local dimensioning within a section subjected to axial force *N* and bending moment *M*. However, buckling is a global phenomenon that affects the entire element rather than individual sections. When considering the effects of second-order (moment amplification factor *M*) and buckling sensitivity (effect on axial compression force *N*), the dimensioning criterion becomes more intricate due to the following factors:

- It involves a comprehensive assessment of the entire element, extending beyond localized section analysis.
- The moment diagram M can exhibit any shape, influencing the amplification factor.
- Section plasticization may occur earlier than anticipated since both first-order and second-order moments accumulate.
- Buckling can manifest in various forms, such as oblique bending or torsion, depending on the section type.
- Axial force N and flexural rigidity EI can undergo variations along the length of the element, presenting spatial changes within the structural member.
- For ductile materials, designers typically adhere to the following dimensioning criterion:

$$\sigma = \frac{\gamma|N|}{A\sigma_{crit}} + \frac{\gamma\left(|M| \Big/ \frac{1-\gamma|N|}{F_{crit}}\right)}{Wf_e} \leq 1 \tag{21}$$

Where:

M: Moment at the middle location of the element

$F_{crit} = \frac{\pi^2 EI}{{L_f}^2}$; Fcrit represents the critical load

$\sigma_{crit} = \frac{F_{crit}}{A}$ or normalized stress curve

γ: Safety coefficient

W: Flexural modulus

Using either the corrected Euler's law or a normalized stress curve, we calculate σ_{crit}. In this section, we explore different combinations of forces *(N_{max}, M_{max})* that lead to maximum stress reaching the material's yield strength f_e in a section subjected to combined bending. We specifically consider the compressive axial force (N>0 in compression) for the analysis.

Let us consider Figure 24 in our analysis. The section crossing point *B* location is particularly significant as it experiences the highest stress. The section is subjected to compressive stress from the bending moment *M* and axial force *N*. In contrast, the section crossing point *A* location experiences comparatively lower stress due to the tension generated by the moment that counteracts the compressive effect of the axial force. Our primary focus is to analyze the section area that produces the maximum compressive stress. Equation (22) represents this maximum compressive stress within section crossing point *B*, considering the predominant influence of combined bending without incorporating the safety factor. Let us start with Equation (22), which expresses the maximum compression stress at point *B*:

$$\sigma_{max}\ \text{Compression at B} = \frac{|N|}{A} + \frac{|M|}{w} \leq f_e \tag{22}$$

When considering second-order buckling effects and safety considerations, Equation (22) is modified to:

$$\frac{\gamma|N|}{A\sigma_{crit}} + \frac{\gamma\left(|M| \Big/ \frac{1-\gamma|N|}{F_{crit}}\right)}{Wf_e} \leq 1 \tag{23}$$

In the case where we restrict the bending stress to the limit buckling stress $\sigma_{crit}=f_e$, Equation (27) can be simplified as:

$$\frac{\gamma|N|}{A\sigma_{crit}} + \frac{\gamma\left(|M| \Big/ \frac{1-\gamma|N|}{F_{crit}}\right)}{Wf_e} \leq 1 \tag{24}$$

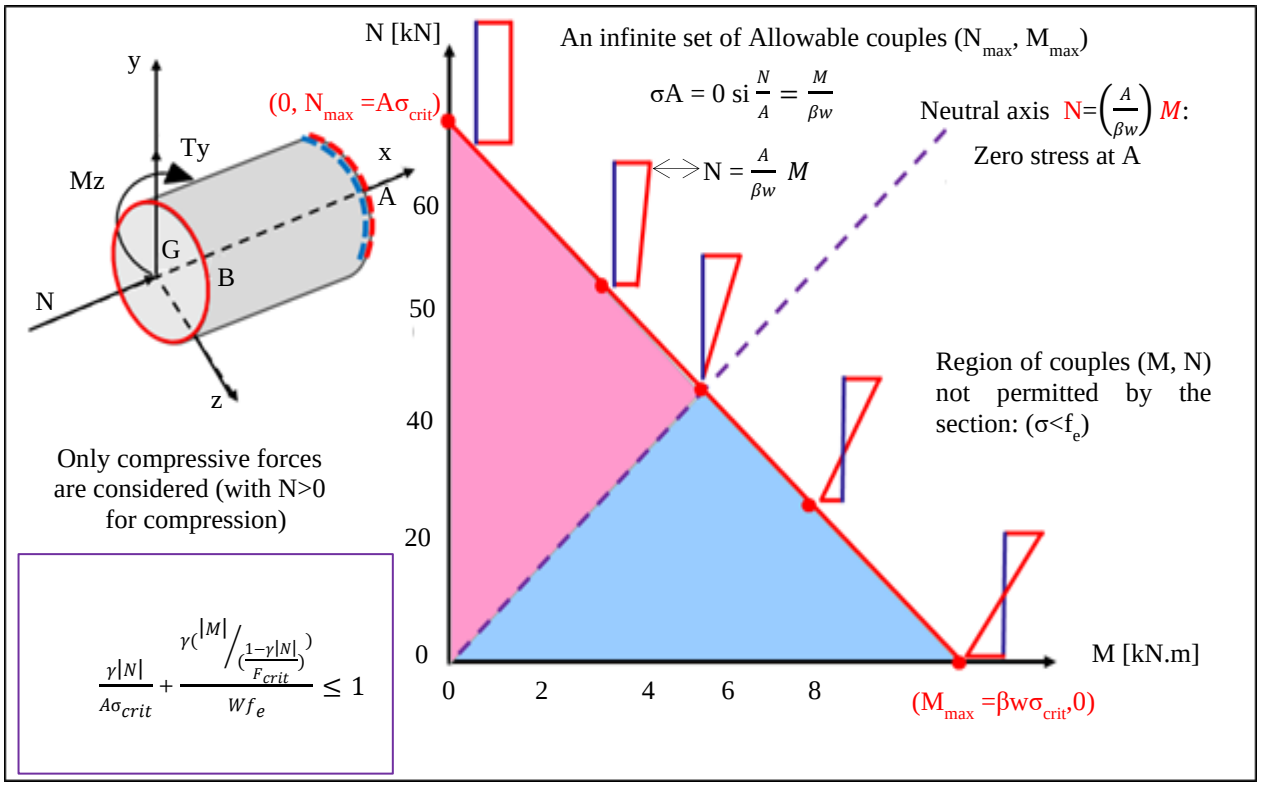

Fig. 26 An infinite set of allowable couples (N_{max}, M_{max}) analysis and state limits representation

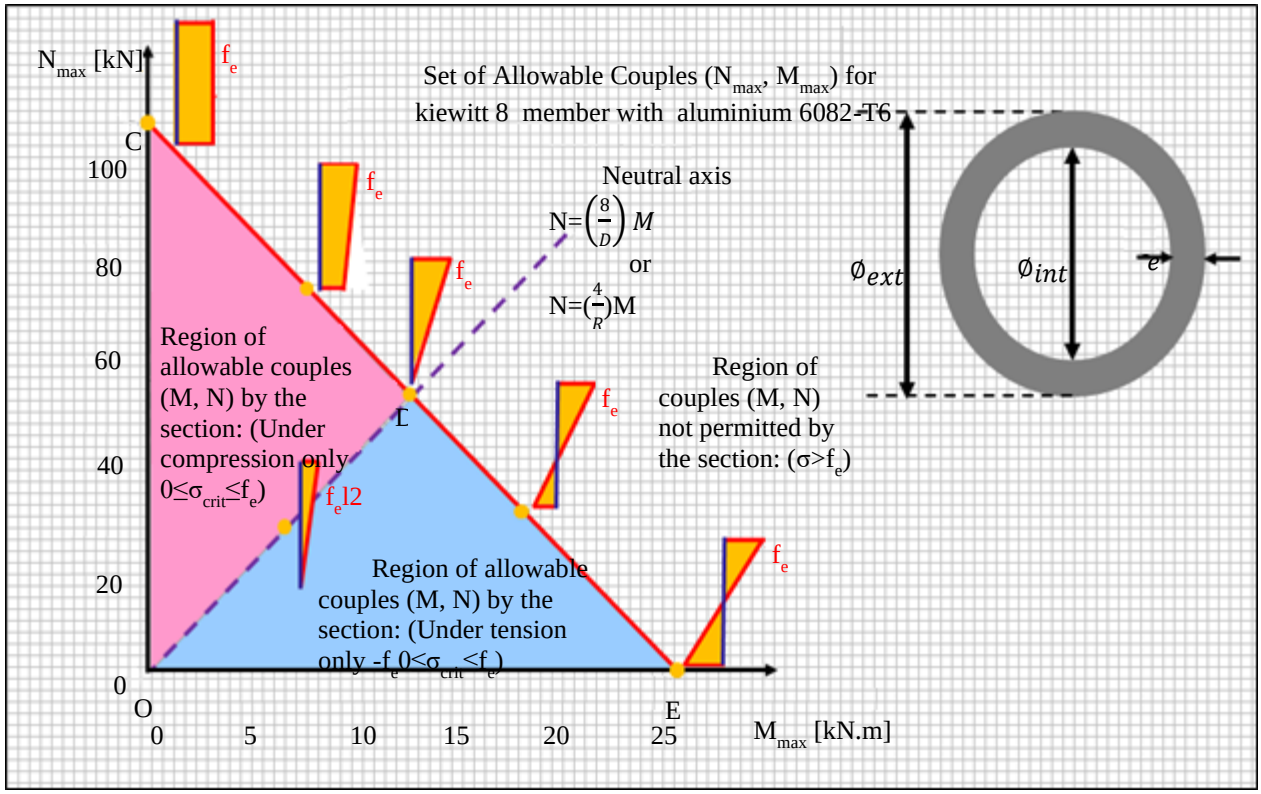

Fig. 27 Set of allowable couples (N_{max}, M_{max}) analysis for kiewitt members with rigid joints

Now, let us introduce a variable:

$$\beta = \frac{1-\gamma|N|}{F_{crit}} \quad (25)$$

With this notation, Equation (25) can be rewritten as:

$$N = A\left(\sigma_{crit} - \frac{1}{\beta W}M\right) \quad (26)$$

Therefore, the coefficient β considers material safety, imperfections, and disturbances contributing to second-order buckling. Next, we will generate a graphical representation depicting the correlation between the regular forces and moments exerted on the section.

The abscissa represents the applied moments, while the y-axis represents the corresponding regular forces. Within this context, we have identified two specific combinations (Nmax and Mmax) representing the section's limit states (see Figure 24). Analyzing Figure 24, we can observe that regarding pure compression, without any moments, the limit combination occurs at point C, where $(N_{max}=A\sigma_{crit}, 0)$.

Conversely, in the scenario of pure bending, without regular forces, the limit combination is found at point *E*, represented by $(0, M_{max}=\beta W\sigma_{crit})$. It is essential to note that exceeding the compression limit $N_{max}=A\sigma_{crit}$ at point C or surpassing the bending moment limit $M_{max}=\beta W\sigma_{crit}$ at point *E* leads to surpassing the critical stress and exceeding the material limit (f_e).

In order to determine the function representing the combinations (M_{max}, N_{max}) that result in reaching the material limit (f_e) on the section crossing point *B* location, we can set Equation (27) to zero. Introducing the following notation:

$$\frac{\gamma|N|}{A\sigma_{crit}} + \frac{\gamma\left(\left|M\right| \Big/ \frac{1-\gamma|N|}{F_{crit}}\right)}{W\sigma_{crit}} = 0 \quad (27)$$

We can derive the equation (26). Here, the value of β corresponds to the expression defined in Equation (25), which considers material safety factors and various imperfections and disturbances contributing to second-order buckling.

The equation represented by Equation (26) corresponds to a straight line in the *(M, N)* coordinate system with a slope of *-A/βW*. This line, depicted in red in Figure 25, crosses the *C* and *E* locations, which represent the limits of pure compression $(N_{max}=A\sigma_{crit}, 0)$ and pure bending $(0, M_{max}=\beta W\sigma_{crit})$, respectively.

It delineates the correlation between the maximum moments and regular forces that allow the material limit f_e to be reached precisely on the section crossing *B* location.

In Figure 25, the upper portion of the curve represents situations where the dominant force is the normal force, resulting in pure compression within the section. In the lower part of the curve, the dominant factor is the bending moment, leading to tension and compression in different regions.

At point *D*, there is a specific combination of couples with zero stress at point A and maximum compression (f_e) at point *B*. Additionally, all points located within the bounds of the triangle *(OCE)* on the curve in Figure 25 correspond to combinations of couples *(N, M)* that do not exceed the material limit (f_e) anywhere, neither on the crown of the section crossing *A* location nor on the one crossing point *B*.

On the other hand, points above the line crossing *C*, *D*, and *E* locations represent combinations of couples *(N, M)* where the material limit (f_e) is exceeded on the section crossing point *B*, and sometimes also on the one crossing point *A*.

We can also consider the points representing stress planes intersecting the section at point *A*, where the stresses are zero on the section crossing that point.

The stress is zero when the compressive stress *(N/A)* is precisely balanced by the bending stress *(M/βW)*. These results in an affine line equation in the *(N, M)* coordinate system with a slope of *(A/βW)*. The dotted purple line crossing *O* and *D* locations encompasses all combinations of couples *(N, M)* that generate a diagram showing only compression within the section, with zero stress on the section crossing point A.

Points along the segment *(OD)* indicate situations where the compressive effect is below the material limit (f_e) on the section crossing point *B*. Point *C* corresponds to combination *(N, M)* where compression occurs throughout the section, with maximum compression at point B.

Points above this line after point *D* represent combinations *(N, M)* that result in compression throughout the section, with zero stress at point *A* and stress levels surpassing (f_e) on the section crossing point *B*. Figure 26 provides an overview of all allowable combinations. The red triangle area *(OCD)* represents fully compressed sections with maximum compressive stress on section crossing point *B*, staying below the material limit (f_e).

The blue triangle area *(ODE)* corresponds to sections experiencing compression and tension, with stresses at *A* and *B* locations below the material limit (f_e) and peak stress at *B* locations.

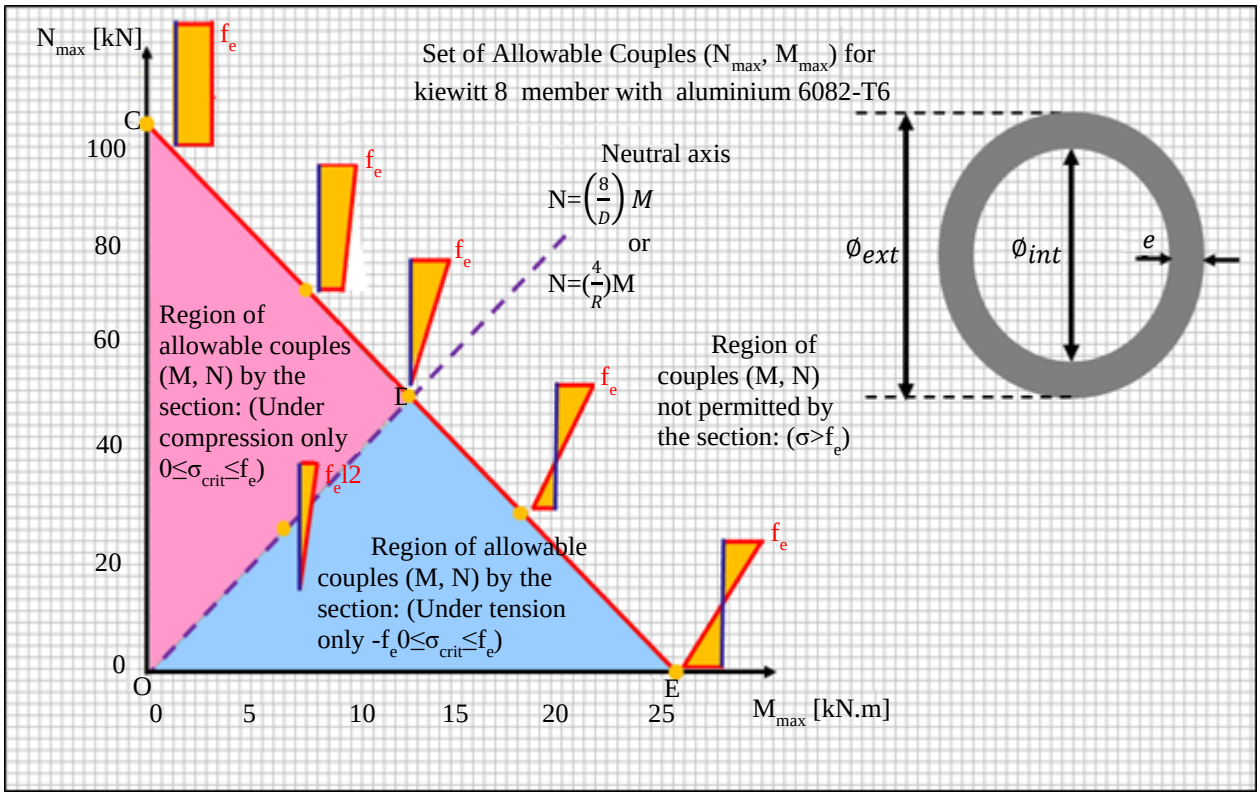

Fig. 28 Set of allowable couples (N_{max}, M_{max}) analysis for kiewitt members with Al. joints

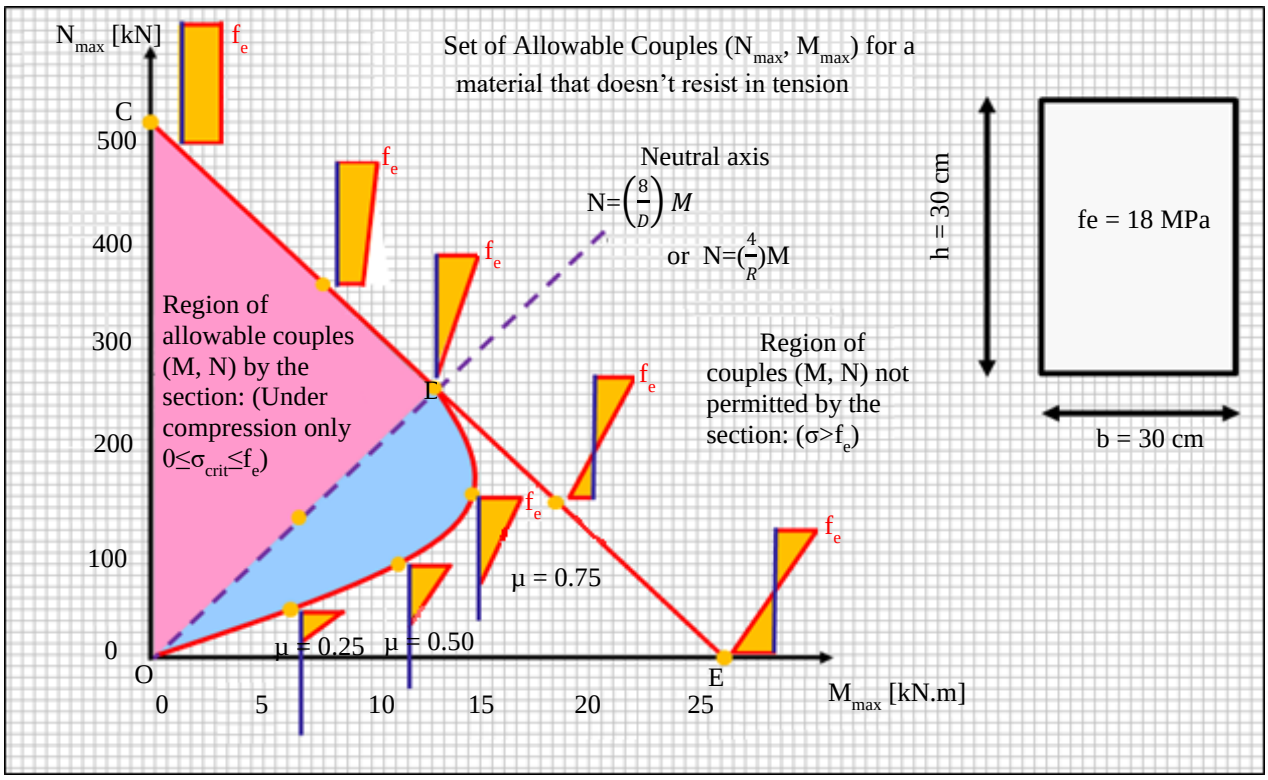

Fig. 29 Set of allowable couples (N_{max}, M_{max}) corrected for kiewitt members with a material unable to withstand tension and rigid joints

The line *(CE)* encompasses all ultimate combinations *(N, M)* that result in ultimate stress crossing *B* location, below the material limit (f_e), and potentially maximum at point *A* during pure bending at point *E*. Known as the ultimate design limit line (Limit State), it delineates the limit. Beyond the ultimate design limit line lies the white area, representing combinations of couples *(N, M)* that yield an ultimate stress surpassing the material limit (f_e) on the section crossing *B* location and possibly on the section crossing point *A*.

This region encompasses combinations leading to excessive compression or unacceptable tension in the material and section. The violet-coloured dashed line serves as a clear indicator, separating the red triangle *(OCD)* from the blue triangle *(ODE)*, enabling a straightforward assessment of whether the section is entirely compressed or subjected to tension. It proves particularly valuable when dealing with a material incapable of withstanding tension. When an element is under combined bending, it can assume infinite couples *(N, M)* combinations. Some combinations solely result in compression within the section (red zone: triangle *(OCD)*), while others involve both compression and tension (blue zone: triangle *(ODE)*).

Certain combinations lead to a limit state within the section, where the material limit (f_e) is reached at either point *A* or *B*. Furthermore, combinations exist beyond the ultimate design limit line, signifying scenarios in which the material limit (f_e) is surpassed. Figures 27 and 28 present the complete range of allowable combinations *(N, M)* for the Aluminium members of the Kiewitt 8 dome structure, considering both rigid and semirigid configurations. These combinations were obtained through a detailed GMNA analysis using Ansys, which carefully incorporates material safety considerations and accounts for various imperfections and disturbances that induce second-order buckling. For specific values of moments and regular forces corresponding to these combinations, refer to Table 6. How can we modify the line connecting pure compression to pure bending to address the material's inability to withstand tension?

3.3. Correction of Allowable Couples for a Material that Resists Not to Tension

Let us examine a rectangular section element with dimensions *(bxh)* and a material that lacks tensile strength, such as concrete. Based on Figure 29, in the tensile region of the section, the stresses will result in material fracture, impeding stress propagation. As a result, only the compressive part of the stress plane remains. In a 2D context, where the section has a height of *h*, the centroid lies at a distance of *h/2* from the upper fiber.

Introducing a new parameter, α, we define αh as the height of the compressed zone. For simplicity, let us assume that this compressed region is always triangular, with its resultant located $\alpha h/3$ away from the upper fiber. Exerting a normal force along with a bending moment at the section's centroid, the stresses induced by this combination *(N, M)* at the centroid (which are compressive stresses) can be considered equal to the stress resulting from the same normal force applied with an eccentricity of $e=M/N$, positioned $\alpha h/3$ away from the upper fiber.

To determine the maximum value of the average load when the compressive stress at the top reaches the material's compressive strength limit f_e, we utilize the following equations:

$$N_{max} = \frac{\alpha h b f_e}{2} \tag{28}$$

And:

$$M_{max} = eN_{max} = \left(\frac{h}{2} - \frac{\alpha h}{3}\right) N_{max} \; ; 0 < \alpha \leq 1 \tag{29}$$

By eliminating α, we obtain a relation between *N* and *M*:

$$M_{max} = \left(\frac{hN_{max}}{2} - \frac{2{N_{max}}^2}{3bf_e}\right) \tag{30}$$

Equation (29) allows for adjusting the line graphically displaying all the limit states of combinations *(N, M)* for sections capable of sustaining tensile forces. Using equation (29), we can identify all the admissible couples *(N, M)* for $\alpha < 1$. When $\alpha = 1$, indicating a purely compressed section, the model presented in Figures 27 and 28 remains applicable. Equation (30) addresses materials that cannot endure tensile forces. It represents a second-degree polynomial that describes a concave parabolic curve with its concavity directed towards negative values of *N*. This curve is depicted in red in Figure 30 and defines the boundary of the lower blue region. It represents the possible states within the section where the maximum compressive stress, f_e, is attained. Conversely, there is no stress in the lower part of the section, as tensile stresses cannot propagate in a cracked section.

This is the corrected blue region shown in Figure 30, encompassing all admissible combinations *(N, M)* for a flexural section composed of a material unable to withstand tension. Consequently, any combinations *(N, M)* in the white region below the correction parabolic curve are invalid. A flexural moment cannot exist without a compensating normal force in a section with a material lacking tensile strength.

Whenever a flexural moment is present in the section, a corresponding normal force is required to maintain force equilibrium and ensure that the maximum stress does not exceed the material's limit, f_e. In other words, in a section with a material unable to withstand tension, the cracking limit of the element can be reached without surpassing the stress limit, f_e, or encountering section instability.

Table 6. Moments and regular forces combinations

Structural Type	K8 with Rigid Joint				
Compressive Load (KN)	0.00	20.00	40.00	60.00	69.24
	73.58	80.00	85.63	85.91	100.00
Moment (KN.m)	25.00	20.00	15.00	10.00	7.69
	6.61	5.00	3.59	3.52	0.00
Structural Type	**K8 with Al. Joint**				
Compressive Load (KN)	0.00	20.00	40.00	49.98	51.49
	60.00	73.19	73.58	80.00	100.00
Moment (KN.m)	25.00	20.00	15.00	12.51	12.13
	10.00	6.70	6.61	5.00	0.00

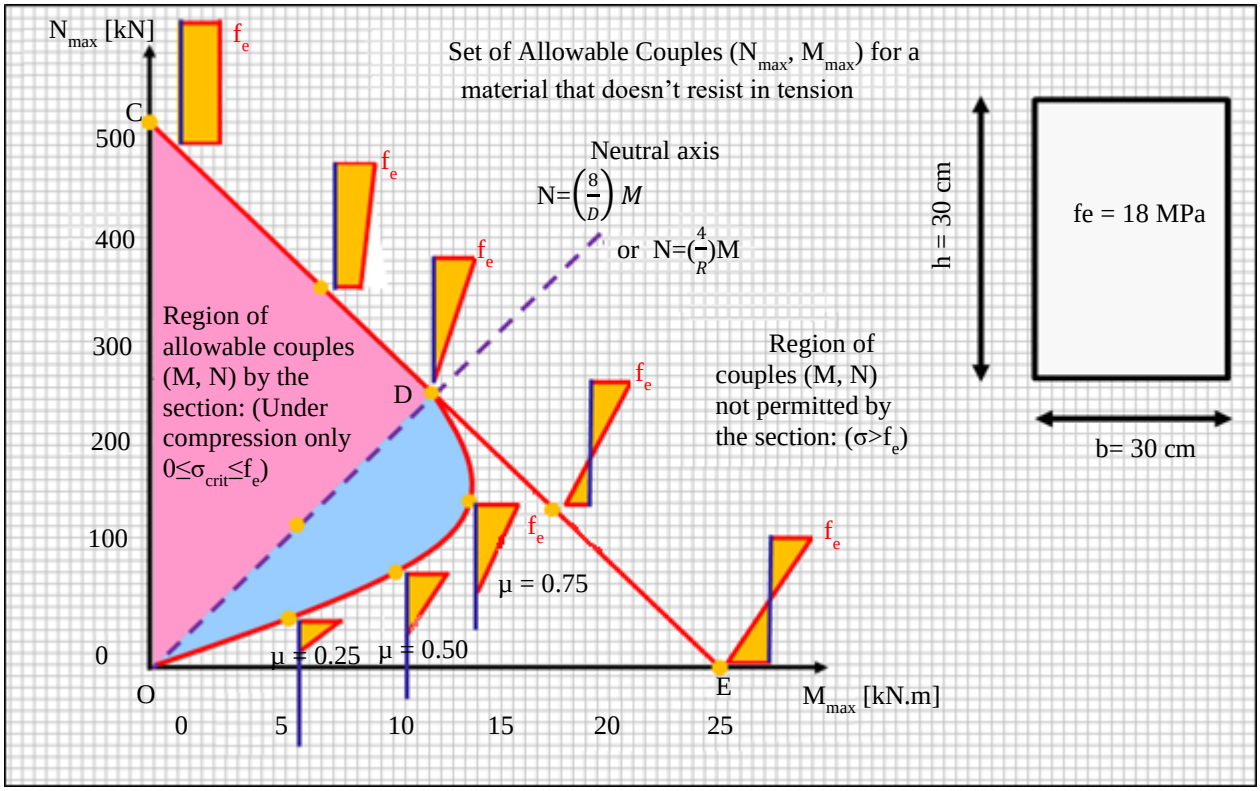

Fig. 30 Set of allowable couples (N_{max}, M_{max}) corrected for kiewitt members with a material unable to withstand tension and semirigid joints

4. Conclusion

In conclusion, this scientific article focuses on the engineering study of designing monolithic dome components using Aluminium 6082-T6 alloy. It provides a comprehensive overview of fundamental concepts related to buckling and their significance in optimizing component design.

The article highlights the importance of buckling in structural design to ensure integrity and safety. It discusses manufacturing imperfections, disturbances, and their impact on second-order effects. The study emphasizes the significance of the *P*-Δ and *P*-*δ* effects in structural behaviour under different loads. Investigating Aluminium 6082-T6 alloy material testing and connection moment capacity in dome structures yields valuable insights. Experimental testing and finite element analysis verification of moment capacity in Aluminium hexagonal joints demonstrate good agreement, enhancing our understanding of their mechanical behaviour.

Design optimization is emphasized, particularly regarding buckling sensitivity and structural integrity. The study highlights the relationship between slenderness ratio and buckling sensitivity, cautioning against high slenderness ratios exceeding 200. The importance of moment of inertia in reducing bending stresses and deformations is also highlighted, suggesting the potential of optimizing material usage. The limitations of Euler's law and the need to consider small slenderness ratios and material yield strength are discussed. The critical slenderness ratio λ_E is identified as the point where Euler's law becomes invalid.

The study emphasizes the necessity of considering permissible stress values based on slenderness ratio and yield strength to ensure structural integrity. Standardization in buckling analysis is stressed for enhancing research credibility and optimizing designs. The study presents standardized buckling curves and equations to calculate critical stress and normalised slenderness ratios, facilitating the consistent investigation and comparison of structural behaviour.

Finally, the study addresses the dimensioning of structural elements subjected to combined bending and buckling forces. It highlights the importance of incorporating second-order effects, buckling susceptibility, and spatial variations in axial force and flexural rigidity. Considering safety coefficients and critical loads, the proposed dimensioning criterion ensures an appropriate utilization ratio and structural integrity. This scientific article provides valuable insights for designing monolithic dome components using Aluminium 6082-T6 alloy.

It emphasizes the significance of considering buckling, optimizing design, understanding Euler's law limitations, and ensuring structural integrity. By incorporating these findings, engineers can enhance the safety and reliability of monolithic dome structures.

Appendix 1 Notation

$M\text{-}\theta$ = Moment-rotation behaviour of the connection;
n = Ring frequency of reticulated dome;
f = Rise of the dome;
L = Span of the reticulated dome;
P = Axial force of the member;
n = Parameter defined by Ramberg-Osgood expression is used to describe the shape of the inelastic portion of the stress-strain diagram
E_0 = Initial Elastic Modulus;
δ_{mid} = Relative bending deflection of the midpoint of the member;
δ_{end} = Relative deflection between the two ends of the member;
$\sigma_{0.1}$ = Nominal yield strength (stress at 0.1 percent plastic strain) or 0.1% proof stress;
$\sigma_{0.2}$ = Nominal yield strength (stress at 0.2 percent plastic strain) or 0.2% proof stress;
σ_u = Ultimate strength;
GNA = Geometric nonlinear analysis;
GMNA = Geometric and material nonlinear analysis;
d = Deflection vector of the dome;
R = radius of curvature;
θ_0 = Half-subtended angle: inclination of the roof for the members at the dome apex;
τ = Ultimate Shear Stress;
σ = Compressive Stress or Ultimate Tensile Stress;
FEM = Finite element model;
σ_{uFE} = Ultimate stress from FEM;
E_0 = Youngs modulus;
K_i = Connection Initial Stiffness;
K_u = Connection Plastic Stiffness;
M_p = Connection Plastic Moment;
M_u = Connection Ultimate Moment;
T18-1, T24-1 & T30-1 = Specimen nominal name in bolts direction;
T18-2, T24-2 & T30-2 = Specimen nominal name perpendicular to bolts direction;
L = domes span;

Appendix 2 List of Figures

Appendix 3 List of Tables

Funding Statement

The authors gratefully acknowledge the financial support for this work from the National Natural Science Foundation of China: Major Building and bridge structures and Earthquake Disaster Integration (91315301).

Data Availability Statement

Some or all data, models, or code that support the findings of this study are available from the corresponding author upon reasonable request.

References

[1] Stephen P. Timoshenko, and James M. Gere, *Theory of Elastic Stability*, McGraw-Hill, 1961. [Google Scholar] [Publisher Link]
[2] Luis A Godoy, "The General Theory of Elastic Stability at the End of the 19th Century," *International Journal of Structural Stability and Dynamics*, vol. 11, no. 3, pp. 401-410, 2011. [CrossRef] [Google Scholar] [Publisher Link]
[3] Bruce W. R. Forde, and Siegfried F. Stiemer, "Improved Arc Length Orthogonality Methods for Nonlinear Finite Element Analysis," *Computers & Structures*, vol. 27, no. 5, pp. 625-630, 1987. [CrossRef] [Google Scholar] [Publisher Link]
[4] Junuthula Narasimha Reddy, *Mechanics of Laminated Composite Plates and Shells: Theory and Analysis*, CRC Press, 2003. [Google Scholar] [Publisher Link]
[5] Xin Chen, and Shi-Zhao Shen, "Complete Load-Defection Response and Initial Imperfection Analysis of Single-Layer Lattice Dome," *International Journal of Space Structures*, vol. 8, no. 4, pp. 271-278, 1993. [CrossRef] [Publisher Link]
[6] Victor Gioncu, "Buckling of Reticulated Shells: State-of-the-Art," *International Journal of Space Structures*, vol. 10, no. 1, pp. 1-46, 1995. [CrossRef] [Google Scholar] [Publisher Link]
[7] J. L. Meek, and Hoon Swee Tan, "Geometrically Nonlinear Analysis of Space Frames by an Incremental Iterative Technique," *Computer Methods in Applied Mechanics and Engineering*, vol. 47, no. 3, pp. 261-282, 1984. [CrossRef] [Google Scholar] [Publisher Link]
[8] Toshiro Suzuki, Toshiyuki Ogawa, and Kikuo Ikarashi, "Elastic Buckling Analysis of Rigidly Jointed Single Layer Reticulated Domes with Random Initial Imperfection," *International Journal of Space Structures*, vol. 7, no. 4, pp. 363-368, 1992. [CrossRef] [Google Scholar] [Publisher Link]
[9] S. Z. Shen, "Design Formulas for Stability Analysis of Reticulated Shells," *Advances in Steel Structures (ICASS'99)*, vol. 1, pp. 51-62, 1999. [CrossRef] [Google Scholar] [Publisher Link]
[10] Shiro Kato, and Tetsuo Yamashita, "Evaluation of Elasto-Plastic Buckling Strength of Two-Way Grid Shells using Continuum Analogy," *International Journal of Space Structures*, vol. 17, no. 4, pp. 249-261, 2002. [CrossRef] [Google Scholar] [Publisher Link]
[11] Feng Fan, Zhenggang Cao, and Shizhao Shen, "Elasto-Plastic Stability of Single-Layer Reticulated Shells," *Thin-Walled Structures*, vol. 48, no. 10, pp. 827-836, 2010. [CrossRef] [Google Scholar] [Publisher Link]
[12] Shiro Kato, Jong-Min Kim, and Myung-Chae Cheong, "A New Proportioning Method for Member Sections of Single Layer Reticulated Domes Subjected to Uniform and Non-Uniform Loads," *Engineering Structures*, vol. 5, no. 10, pp. 1265-1278, 2003. [CrossRef] [Google Scholar] [Publisher Link]
[13] F. A. Fathelbab, *Space Structures 4: Tangent Stiffness Matrix for Space Frame Members with both Member and Joint Imperfections*, Thomas Telford, vol. 2, pp. 1323-1333, 1993. [Google Scholar] [Publisher Link]
[14] A. L. El-Sheikh, "Numerical Analysis of Space Trusses with Flexible Member-End Joints," *International Journal of Space Structures*, vol. 8, no. 3, pp. 189-197, 1993. [CrossRef] [Google Scholar] [Publisher Link]

[15] Aitziber López, Iñigo Puente, and Miguel A Serna, "Numerical Model and Experimental Tests on Single-Layer Latticed Domes with Semi-Rigid Joints," *Computers & Structures*, vol. 85, no. 7-8, pp. 360-374, 2007. [CrossRef] [Google Scholar] [Publisher Link]

[16] Ma H H, Feng Fan, and S. Z. Shen, "Numerical Parametric Investigation of Single-Layer Latticed Domes with Semi-Rigid Joints," *Journal of the International Association for Shell and Spatial Structures*, vol. 49, no. 2, pp. 99-110, 2008. [Google Scholar] [Publisher Link]

[17] Murakami Masumi, and Heki Koichiro, "On the Analysis of Elastic Buckling of Single-Layer Latticed Domes with Regular Hexagonal Plan Under Gravity Load," *Proceedings of International Association for Shell and Spatial Structures 1991 Symposium*, vol. 3, pp. 101-108, 1991. [Google Scholar]

[18] Feng Fan et al., "Experimental Study of Semi-Rigid Joint Systems Subjected to Bending with and without Axial Force," *Journal of Constructional Steel Research*, vol. 68, no.1, pp. 126-137, 2012. [CrossRef] [Google Scholar] [Publisher Link]

[19] Shiro Kato, Itaru Mutoh, and Masaaki Shomura, "Effect of Joint Rigidity on Buckling Strength of Single Layer Lattice Domes," *Spatial, Lattice and Tension Structures*, 1994. [Google Scholar] [Publisher Link]

[20] Shiro Kato, Itaru Mutoh, and Masaaki Shomura, "Collapse of Semi-Rigidly Jointed Reticulated Domes with Initial Geometric Imperfections," *Journal of Constructional Steel Research*, vol. 48, no. 2-3, pp. 145-168, 1998. [CrossRef] [Google Scholar] [Publisher Link]

[21] Shen S. Z, "Stability Analysis of Reticulated Shells in Chinese Technical Specifications," *Association for Progressive Communications 2000*, pp. 237-248, 2000.

[22] Seishi Yamada et al., "Imperfection-Sensitive Overall Buckling of Single-Layer Lattice Domes," *Journal of Engineering Mechanics*, vol. 127, no. 4, pp. 382-386, 2001. [CrossRef] [Google Scholar] [Publisher Link]

[23] Feng Fan, Jiachuan Yan, and Zhenggang Cao, "Elasto-Plastic Stability of Single-Layer Reticulated Domes with Initial Curvature of Members," *Thin-Walled Structures*, vol. 60, pp. 239-246, 2012. [CrossRef] [Google Scholar] [Publisher Link]

[24] Jiachuan Yan, "*Mechanism of Coupled Instability of Reticulated Shell Structures with Initial Curvature of Members*," Harbin Institute of Technology, 2012.

[25] Jiachuan Yan et al., "Mechanism of Coupled Instability of Single-Layer Reticulated Domes," *Engineering Structures*, vol. 114, pp. 158-170, 2016. [Google Scholar] [Publisher Link]

[26] Siu Lai Chan, and Zhi Hua Zhou, "Second-Order Elastic Analysis of Frames Using Single Imperfect Element per Member," *Journal of Structural Engineering*, vol. 121, no. 6, pp. 939-945, 1995. [CrossRef] [Google Scholar] [Publisher Link]

[27] Siu-Lai Chan, and Jian-Xin Gu, "Exact Tangent Stiffness for Imperfect Beam-Column Members," *Journal of Structural Engineering*, vol. 126, no. 9, pp. 1094-1102, 2016. [CrossRef] [Google Scholar] [Publisher Link]

[28] LI Guo-qiang, and LIU Yu-shu, "A Nonlinear Beam Element Considering Initial Imperfection," *Chinese Journal of Computational Mechanics*, vol. 22, no. 1, pp. 6-7, 2005. [Publisher Link]

[29] C. Su, "Research on the Limited Capacity of Rigid Large-Span Steel Space Structures," *Shanghai: Tongji University*, pp. 37-42, 2006.

[30] Zhou Z, S. Meng, and J. Wu, "Nonlinear Link Element Considering Member Initial Curvature," *Journal of Southeast University (Natural Science Edition)* vol. 37, no. 2, pp. 201-205, 2007.

[31] Huan-Chun Sun, Y. F. Wang, and Chun-Liang Liu, "Geometric Nonlinear Eulerian Stability Theory for the Stability," *Chinese Journal of Computational Mechanics*, vol. 24, no. 4, pp. 539-544, 2007.

[32] GB6397 86, *Metal Tensile Test Specimens*, 1986.

[33] Guy Oyéniran ADEOTI et al., "Investigation of Aluminium Bolted Joint (HBJ) System Behavior," *Thin-Walled Structures*, vol. 144, p. 106100, 2019. [CrossRef] [Google Scholar] [Publisher Link]

[34] J. M. T. Thompson, "Basic Principles in the General Theory of Elastic Stability," *Journal of the Mechanics and Physics of Solids*, vol. 11, no. 1, pp.13-20, 1963. [CrossRef] [Google Scholar] [Publisher Link]

[35] European Standard, "*Design of Steel Structures, Parts16: Strength and Stability of Shell Structures*," Brussels: European Committee for Standardization, 2004.

[36] Iradj M. Kani, and Richard E. Mc Connel, "Collapse of Shallow Lattice Domes," *Journal of Structural Engineering*, vol. 113, no. 8, pp. 1806-1819, 1987. [CrossRef] [Google Scholar] [Publisher Link]

[37] Iradj M. Kani, and Richard E. Mc Connel, "Single Layer Shallow Lattice Domes: Analysis, General Behaviour and Collapse," *International Journal of Space Structures*, vol. 3, no. 2, pp. 64-73, 1988. [CrossRef] [Google Scholar] [Publisher Link]

[38] K. Abedi, and G. A. R. Parke, "Progressive Collapse of Single-Layer Braced Domes," *International Journal of Space Structures*, vol. 11, no. 3, pp. 291-306, 1996. [CrossRef] [Google Scholar] [Publisher Link]

[39] Huihuan Ma et al., "Numerical Simulation of Semi-Rigid Joints in Single-Layer Dome Structures," *Journal of the International Association for Shell and Spatial Structures*, vol. 52, no. 1, pp. 3-18, 2011. [Google Scholar] [Publisher Link]

[40] Feng Fan, Jiachuan Yan, and Zhenggang Cao, "Stability of Reticulated Shells Considering Member Buckling," *Journal of Constructional Steel Research*, vol. 77, pp. 32-42, 2012. [CrossRef] [Google Scholar] [Publisher Link]

[41] Huihuan Ma et al., "Stability Analysis of Single-Layer Elliptical Paraboloid Latticed shells with Semi-Rigid Joints," *Thin-Walled Structures*, vol. 72, pp. 128-138, 2013. [CrossRef] [Google Scholar] [Publisher Link]

[42] Huihuan Ma et al., "Experimental and Numerical Studies on a Single-Layer Cylindrical Reticulated Shell with Semi-Rigid Joints," *Thin-Walled Structures*, vol. 86, pp. 1-9, 2015. [CrossRef] [Google Scholar] [Publisher Link]

[43] Guy Oyeniran Adeoti et al., "Stability of 6082-T6 Aluminium Alloy Columns with H-Section and Rectangular Hollow Sections," *Thin-Walled Structures*, vol. 89, pp. 1-16, 2015. [CrossRef] [Google Scholar] [Publisher Link]

[44] Guy Oyeniran Adeoti et al., "Review on Aluminium and Steel Semi-Rigid Connections Behavior Design Model," *Civil Engineering and Architecture*, vol. 09, no. 01, pp. 184-205, 2021. [CrossRef] [Google Scholar] [Publisher Link]

[45] Guy Oyeniran Adeoti et al., "Optimum Design and Stability of Rigid and Semi-Rigid Reticulated Dome Members," *Civil Engineering and Architecture*, vol. 11, no. 05, 2023.

[46] Pierre Latteur, *Calculate A Structure, from Theory to Example*, Digital Access to Libraries, 2016. [Google Scholar] [Publisher Link]

[47] Clough R. W, and Penzien. J, *Dynamics of Structures*, McGraw-Hill NY, 1993.

[48] Pierre Latteur, "*Le Béton Armé Dans Tous Ses Etats*," Academia Bruylant, 2001.

[49] European Committee for Standardization (CEN), Brussels, *Eurocode 9: Design of Aluminium Alloy Structures: General Rules*, 1998.

[50] European Committee for Standardization (CEN), Brussels, *Eurocode 3: Design of Steel Structures, Part 1.1: General Rules and Rules for Buildings*, 1992.